Universiteit Utrecht

Department of Physics & Astronomy
Utrecht University

September 19, 2013

Homo-FRET Detection by Fluorescence Polarization Anisotropy in Wide-field Microscopy

Nivard Kagie
Student number: 0488593

Project to complete the master's programme Nanomaterials: Chemistry & Physics
At the Molecular Biophysics group of the Debye Institute

Supervisors: prof. dr. H.C. Gerritsen
dr. G.A. Blab

Abstract

A fluorescence wide-field microscope setup for simultaneous detection of the parallel and perpendicular intensities was used in order to detect homo-FRET between fluorescently labelled proteins, thereby revealing clustering of the biological constructs of interest. Quantitative anisotropy imaging with sub-cellular resolution using seperate detection channels requires high quality registration of the images regarding the data analysis process. Cells expressing green fluorescent protein(GFP) constructs that contain two FKBP binding proteins were used to verify the effect of oligomerization of the constructs to anisotropy. The results show a significant decrease of the anisotropy of $6,5 \pm 1,2\%$ due to homo-FRET upon clustering of the GFP molecules. Determination of the autofluoresence turned out to be a critical factor in wide-field anisotropy measurements, as the absolute anisotropies show an increase of roughly 2% after subtraction of a slightly higher autofluorescence. However, due to the fact that both the clustered and non-clustered anisotropies increased with the same relative amount, the relative decrease hardly changed. Furthermore, when the resolution of the images is reduced by binning the pixels upon imaging, the decrease in anisotropy is lower and the uncertainty is roughly twice as big: $4,4 \pm 2,2\%$. Probably, the quality of the registration diminishes due to the lower resolution of the images and hence the overlay is not perfect, resulting in less reliable anisotropy values.

Contents

List of Figures

Chapter 1

Introduction

The use of fluorescence microscopy has been extensively growing in biological sciences over the past decades. Fluorescence emerged as the dominant methodology in cellular and molecular imaging, especially in studying processes in living cells[28, 38]. Fluorescence imaging can reveal localization and measurements of intracellular molecules, even at the level of single-molecules. However, imaging with light immediately poses a physical limitation: it's diffraction limited, i.e. visualization of structures is restricted to the optical resolution, which is roughly half the wavelength of light. To overcome this resolution limiting problem, more recent developments in super-resolution imaging have become available, where there's technically no limit to the resolution of light microscopy. In practice, many of these super resolution techniques are less suitable for live cell imaging since they usually require long time imaging and intensive processing and illumination.

Several parallel fluorescence, photo-physics based, techniques exist which provide methods to examine inter-molecular interactions. One of the first examples was described by [14] and involved Förster resonance Energy Transfer(FRET) analyzed by Fluorescent Lifetime Imaging Micorscopy(FLIM)[14]. FRET is based on energy transfer between two fluorescent molecules. As the FRET-efficiency depends on the inter-molecular distance, determining the FRET-efficiency is equivalent to measuring distances. Since the typical length scale for FRET is 1 - 10nm, imaging of FRET processes in a cell expands the resolution of light microscopy beyond the diffraction limit, thereby providing nanoscale informations about interactions between molecules. Different methods can be applied in order to detect FRET, for example by measuring the changes in the fluorescence lifetime(FLIM) of the involved molecules. Also fluorescence polarization anisotropy can be used to detect FRET, where the loss of the polarization state of emitted fluorescence due to FRET is measured. However, FLIM can only be used for energy transfer between different molecules(hetero-FRET), wheras fluorescence polarization anisotropy can be used for detection of FRET between identical molecules as well(homo-FRET).

1.1 This thesis

The methodology for homo-FRET detection, fluorescence polarization anisotropy, is the focus of research in this report. Homo-FRET experiments have already been successfully performed on a confocal microscope by [4], by means of time-resolved and steady-state anisotropy measurements. However, the experiments are time-consuming, since confocal microscopy requires

imaging of a sample on a pixel per pixel basis. Another disadvantage with respect to wide-field imaging is the low intensity, and hence low signal-to-noise ratio, arising from confocal microscopy as the pinhole is responsible for the rejection of the out-of-focus light.

In this thesis, we'll provide a wide-field fluorescence polarization anisotropy method for detecting homo-FRET, which enables measuring on relatively short time-scales combined with a high signal-to-noise ratios. Furthermore, the whole procedure of setting up wide-field experiments as well as the key paramaters for ensuring high quality results, including data handling and analysis, will be discussed in order to provide a guideline for wide-field polarization anisotropy imaging.

1.1.1 Epidermal growth factor receptor

The ultimate goal of this research project is to determine clustersizes in biological samples. After establishing the setup and confirming its proper working by imaging biologically 'straight-forward' samples, we will examine more advanced and scientifically relevant constructs. In collaboration with the biology department of the Utrecht University, we investigated the behaviour of the epidermal growth factor receptor(EGFR), which is located on the membrane of the cell. This is a well-studied receptor as many types of cancers exhibit overexpression of EGFR. It turned out that activation of EGFR is very important in several cell processes, like cell growth and cell migration[27, 34]. Since a mechanistic understanding of EGFR activation in a tumor cell requires knowledge of the spatial organization of the receptor on the cell surface, homo-FRET experiments could reveal details about the mechanisms leading to activation of EGFR. So ultimately, we would like to perform anisotropy measurements on several types of EGFR constructs in order to determine whether clustering of the cell membrane receptor has taken place.

Chapter 2

Theoretical Background

2.1 Fluorescence

The emission of light, luminescence, is the result of radiative decay from electronically excited states, which can be divided in fluorescence and phosphorescence. In an excited singlet state, the electron in the excited state is paired to the electron in the ground state, i.e. the spins are opposite. As a consequence, the decay from excited state to ground state is allowed and hence the transition, involving emission of a photon, is rather fast. The fluorescence lifetime is typically 1 - 10 ns. In contrast, phosphorescence comprises emission from a triplet state, in which the electrons have the same spin. Therefore, the transition is spin forbidden and so the lifetime is much larger, typically milliseconds to seconds.

The process of absorption and fluorescence emission is shown in figure 2.1. We immediately recognize one of the main characteristics of fluorescence: the Stokes-shift, i.e the energy of emission is lower than the energy of absorption. Typically, absorption occurs to higher vibrational levels of the excited singlet states, after which relaxation to the lowest vibrational level occurs rapidly(in the order of 10^{-12} s). Moreover, radiative decay occurs from this lowest vibrational level of S_1 to one of the higher vibrational levels of S_0. So it's these two components that are responsible for the Stokes-shift.

Moreover, the polarization of the emitted light depends on the orientation of the dipole moment of the involved transition. The electric field vector of the fluorescence light will therefore be oriented along the axis of this dipole moment and hence the emission of light upon fluorescence from a single molecule is linearly polarized. It's exactly this feature of fluorescence that enables its use in homo-FRET experiments, as we will see in the next sections.

2.2 Förster Resonance Energy Transfer

A fluorophore in an excited state, the donor, is able to transfer its energy to a nearby acceptor molecule. This process is called Förster Resonance Energy Transfer, FRET. It's important to realize that there's no photon involved in energy transfer, but instead the donor and acceptor are coupled via a dipole-dipole intereaction. There are three requirements for the involved fluorophores in order to create good conditions for FRET: (1) the emission spectrum of the donor should overlap with the absorption spectrum of the acceptor, (2) the donor and acceptor
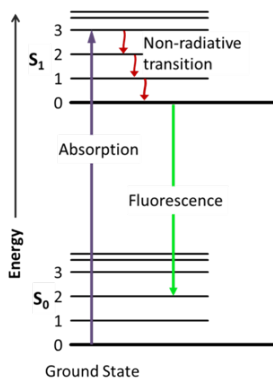
Figure 2.1: A Jablonski diagram: schematic representation of fluorescence emission. Absorption typically occurs to higher vibrational levels of the excited singlet states, whereas emission occurs from the lowest excited state to one of the higher vibrational levels of the ground state: yielding the Stokes-shift.

need to be close together and (3) the donor's emission and the acceptor's absorption dipole moments are not perpendicularly oriented.

The FRET efficiency is extremely sensitive to small changes in distance since it is inversely proportional to the sixth power of the distance between the fluorophores

$$E = \frac{R_0^6}{R_0^6 + R^6} \tag{2.1}$$

with R the distance between donor and acceptor and R_0 being the Förster distance, which depends on the spectral overlap of the donor's emission spectrum and the acceptor's absorption spectrum and represents the distance at which the energy transfer efficiency is 50%. The Förster distance is defined as

$$R_0^6 = \frac{9Q_0 \kappa^2 \ln(10) J(\lambda)}{128\pi^5 n^4 N_A} \tag{2.2}$$

where Q_0 is the fluorescence quantum yield of the donor in absence of the acceptor, n the refractive index of the medium, N_A Avagadro's number and $J(\lambda)$ the spectral overlap integral. The parameter κ^2 denotes the dipole orientation factor, which describes the angular alignment between the emission dipole moment of the donor and the absorption dipole moment of the acceptor. For a random directional distribution of fluorophores, $\kappa^2 = 2/3$ [35]. Typical values for R_0 are between 1 and 10 nm[36] and hence fluorophores need to be within a distance of approximately 10 nm in order to get significant energy transfer.

2.3 Homo-FRET

In the previous section we discussed the principles of resonance energy transfer between fluorophores. In general we can distinguish two types of energy transfer. In case of different donor and acceptor molecules we speak of hetero-FRET, whereas homo-FRET is used for energy transfer between identical molecules. Upon hetero-FRET, the donor emission quenches and

emisison from the acceptor is enhanced. This means that the efficiency can be determined by measuring the donor/acceptor intensity ratio or by using spectral imaging. Moreover, Fluorescence Lifetime Imaging(FLIM) is a reliable tool for measuring the FRET efficiency[12, 37]. T he lifetime is defined as the time after which the fluorescence intensity has dropped to 1/e of the initial intensity, quenching of the donor emission leads to a decrease in lifetime, making FLIM an effective way of determining the FRET-efficiency.

The above mentioned conditions for FRET can also be met for a pair of identical fluorophores, as significant spectral overlap of the emission and absorption spectrum of a fluorophore is often observed[16, 19, 31, 38]. However, the discussed methods involving differences in spectral properties, i.e. intensity ratio and spectral imaging, used for hetero-FRET are obviously not suitable for imaging homo-FRET. Furthermore, the lifetime upon homo-FRET doesn't change, as the decrease in emission from the donor is fully compensated by emission from the acceptor. However, measuring the anisotropy, i.e. the emission polarization of the fluorophores, reveals energy transfer between identical donor and acceptor molecules and hence this serves as a tool for detecting both homo- and hetero-FRET.

2.3.1   Detection of homo-FRET: Fluorescence anisotropy

The fluorescence anisotropy can be determined by measuring the polarization of the emission light. If two orthogonal directions of polarization are defined, parallel and perpendicular with respect to the excitation light, and their intensities are measured, the anisotropy, r, follows from its definition

$$r = \frac{I_\parallel - GI_\perp}{I_\parallel + 2GI_\perp} \tag{2.3}$$

where, $I_\parallel$ and $I_\perp$ represent the parallel and perpendicular intensities respectively and G is a factor that accounts for a preferential polarization in the setup, which will be clarified later on. In an ideal setup, G would be equal to 1 and so could be left out of the defintion. The factor two in the denominator shows up because the total intensity, which acts as a normalization factor, is the sum of the parallel and perpendicular intensities, with equal contributions from the two perpendicular directions. A detailed derivation of the terms in (2.3) is given in appendix A.

When a sample of fluorophores is illuminated with linearly polarized light, those fluorophores with an absorption dipole moment aligned with the excitation light have the highest probability of being excited. Without energy transfer between molecules and other depolarizing factors, the emission will be polarized as well. Now, if we consider a randomly oriented ground state distribution, the neighbouring molecules, available for energy transfer, will have a random orientation relative to the excited molecules. Hence, after energy transfer the emission will be depolarized with respect to the polarization without energy transfer, as shown in figure 2.2 for GFP-molecules embedded in the membrane.

2.4   Quantification of clustersize

As we have just seen, the anisotropy decreases upon energy transfer between donor and acceptor and so anisotropy measurements can be used to detect homo-FRET and thus clustering of fluorescent molecules. However, we've only shown the depolarizing effect of FRET qualitatively and intuitively, but not yet in a quantitative manner. In this section we will derive
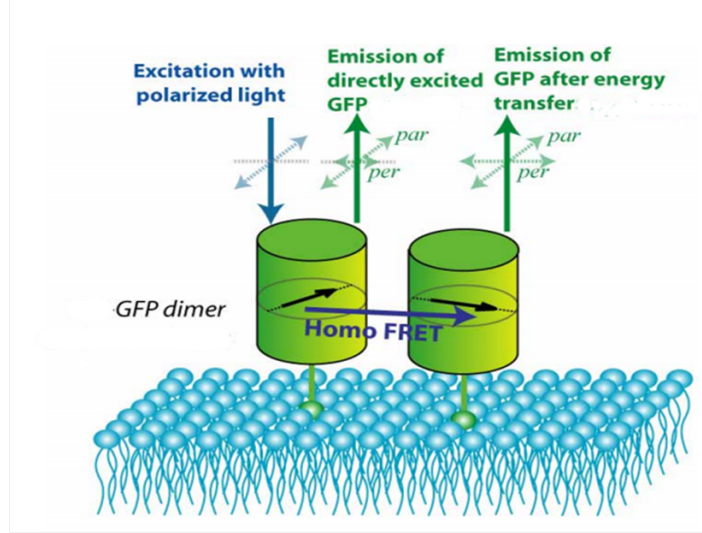
Figure 2.2: Schematic drawing of depolarization due to energy transfer in a GFP dimer. The left molecule is excited by the excitation light, as its absorption dipole moment is aligned to the polarized excitation. After energy transfer within the lifetime of the molecule, the right molecule emits a photon with a slightly different polarization due to its orientation.

anisotropy expressions for clusters of fluorophores by discriminating between emission from the donor and emission from the acceptor. When we speak of the term 'cluster' we mean a set of molecules interacting together as a group, while only interactions between neighbouring molecules, on the length scale of FRET, are considered.

The key point in this derivation is the determination of the quantum yield of each fluorophore by considering its decay probability. Hereby, the relative contributions of both donor and acceptor to the anisotropy are calculated.

2.4.1   N=1 single molecule

After excitation, the molecule will be in the excited state for a finite time, depending on its lifetime τ. Besides the natural lifetime, τ_0, of the fluorophore we have got other, non-radiative, sources of de-excitation, with a rate k_{nr}. Together they form the average lifetime, defined as $\frac{1}{\tau} = (\frac{1}{\tau_0} + k_{nr})$. We can set-up a differential equation for the probability $\rho(t)$ that the molecule is in the excited state, with boundary conditions $\rho(t = 0) = 1$ and $\rho(t = \infty) = 0$, and solve it [13]

$$\frac{\partial \rho(t)}{\partial t} = -(\frac{1}{\tau_0} + k_{nr}) \cdot \rho(t) \Rightarrow \rho(t) = e^{-t/\tau} \tag{2.4}$$

Integration of the probability over time gives the quantum yield ϕ of the system

$$\phi = \frac{1}{\tau_0} \int_0^\infty \rho(t) \cdot \mathrm{d}t = \frac{\tau}{\tau_0} \tag{2.5}$$

Figure 2.3: Interactions between initially excited molecule j and the randomly oriented indirectly excited molecule k, where F_{jk} and F_{kj} represent the rates of energy transfer from molecule j to k and vice versa.

So we see that any nonradiative decay results in a decrease of the average lifetime and thus of the quantum yield.

2.4.2   N=2 cluster

For two molecules, j and k, forming a cluster, so exhibiting energy transfer, the probability functions, ρ_j and ρ_k respectively, are coupled. As energy transfer means de-excitation of the donor and excitation of the acceptor, they influence each other. For this case we can set the following boundary condition for excitation of molecule j at t=0: $\rho_j(t = 0) = 1$, $\rho_j(t = \infty) = 0$, $\rho_k(t = 0) = 0$ and $\rho_k(t = \infty) = 0$. The decay rate of ρ_j and ρ_k will be proportional to the transfer rates, F_{jk} and F_{kj}(see figure 2.3), between them. Hence, the changes in decay of the probabilities are given by

$$\frac{\partial \rho_j(t)}{\partial t} = -\frac{\rho_j(t)}{\tau} - F_{jk}\rho_j(t) + F_{kj}\rho_k(t) \tag{2.6}$$

$$\frac{\partial \rho_k(t)}{\partial t} = -\frac{\rho_k(t)}{\tau} - F_{kj}\rho_k(t) + F_{jk}\rho_j(t) \tag{2.7}$$

Of course, we're dealing with homo-FRET so F_{jk} and F_{kj} are equal. From [13] we know that the rate of energy transfer between fluorophores is given by

$$F = F_{jk} = F_{kj} = \frac{1}{\tau} \cdot (\frac{R_0}{R_{jk}})^6 \tag{2.8}$$

The general solutions to (2.6) and (2.7) for $\rho_j(t)$ and $\rho_k(t)$ can now be given in terms of (2.8)

$$\rho_j(t) = 1/2 \cdot (1 + e^{-2 \cdot F \cdot t}) \cdot e^{-t/\tau} \tag{2.9}$$

$$\rho_k(t) = 1/2 \cdot (1 - e^{-2 \cdot F \cdot t}) \cdot e^{-t/\tau} \tag{2.10}$$

We immediately notice that the individual probabilities add up to the probability for a single molecule, as given by (2.4). Of course, we would expect the quantum yield of the cluster to be the same as for the single molecule. So, obviously, the quantum yield of the cluster doesn't change upon homo-FRET. Energy transfer only affects the quantum yield of the individual molecules, and hence the anisotropy decreases, as the emission from the indirectly excited molecule is depolarized with respect to the initially excited molecule.

If we consider the homo-FRET efficiency to be high, i.e. multiple energy transfer processes take place within the lifetime of the molecule, energy is transferred back and forth between donor and acceptor. In this way, a dynamic system of energy exchange is created in which equilibrium is established between all molecules in the cluster. Thus the emission of the cluster has two components: emission from the initially excited donor and depolarized emission from the neighbouring molecule that is excited via energy transfer. That means that we need to know the quantum yield arising from both molecules in the $N = 2$ cluster in order to calculate the total anisotropy.

$$\phi_j = \frac{1}{\tau_0} \int_0^\infty \rho(t) \cdot \mathrm{d}t = \phi_{tot} \frac{1 + \tau \cdot F}{1 + 2 \cdot \tau \cdot F} \tag{2.11}$$

$$\phi_k = \frac{1}{\tau_0} \int_0^\infty \rho(t) \cdot \mathrm{d}t = \phi_{tot} \frac{\tau \cdot F}{1 + 2 \cdot \tau \cdot F} \tag{2.12}$$

where ϕ_{tot} denotes the quantum yield of the cluster. If we now define two terms, r_1 and r_{et}, for the anisotropy arising from the initially excited molecule and the acceptor respectively, we find the total anisotropy of the cluster in terms of the quantum yield of each fluorophore relative to the quantum yield of the cluster

$$r_{tot} = r_1 \cdot \frac{\phi_j}{\phi_{tot}} + r_{et} \cdot \frac{\phi_k}{\phi_{tot}} = r_1 \cdot \frac{1 + \tau \cdot F}{1 + 2 \cdot \tau \cdot F} + r_{et} \cdot \frac{\tau \cdot F}{1 + 2 \cdot \tau \cdot F} \tag{2.13}$$

Substitution of (2.8) into this expression yields an R-dependent function of the anisotropy, with $R_{jk} = R$

$$r_{tot} = r_1 \cdot \frac{1 + (R_0/R)^6}{1 + 2(R_0/R)^6} + r_{et} \cdot \frac{(R_0/R)^6}{1 + 2(R_0/R)^6} \tag{2.14}$$

When the homo-FRET efficiency is low, which is the case for $(R_0/R)^6 \ll 1$, we see that there's hardly any emission from the acceptor molecule so the anisotropy of the cluster approaches that of a single molecule($r_{tot} = r_1$). On the other hand, if the efficiency is very high, so $(R_0/R)^6 \gg 1$, we see an equal emission probability for either molecules and hence they contribute equally to the anisotropy.

2.4.3 Cluster of size N

In principle, the theory described in the former section for $N = 2$ clusters can be extended to clusters of N molecules. In this case, generalization of (2.6) yields[8]

$$\frac{\partial \rho_j(t)}{\partial t} = -\frac{\rho_j(t)}{\tau} - \sum_{k \neq j}^{N} F_{jk} \cdot \rho_j(t) + \sum_{m \neq j}^{N} F_{mj} \cdot \rho_m(t) \qquad (2.15)$$

Here, the first term describes the excitation decay in the absence of energy transfer. The first summation denotes the sum over all rates of energy transfer from molecule k to all other molecules in the cluster and the last term represents rates of energy transfer back to the donor molecule. Analogous to the derivation for the $N = 2$ cluster, we get N coupled differential equations for a cluster of N interacting molecules. By solving this set of equations and calculating again the quantum yields per molecule we obtain the following general expression for the anisotropy of a cluster of N molecules

$$r_N = r_1 \cdot \frac{1 + \tau \cdot F}{1 + N \cdot \tau \cdot F} + r_{et} \cdot \frac{(N-1)\tau \cdot F}{1 + N \cdot \tau \cdot F} \qquad (2.16)$$

Note that for $N = 2$ this expression is equal to the total anisotropy we found in the former section, given by (2.13). Furthermore, we can again assume the homo-FRET rate to be much faster than the rate of fluorescence, so $\tau \cdot F \Rightarrow \infty$ which is equivalent to $(R_0/R)^6 \gg 1$. Then, (2.16) reduces to

$$r_N = r_{mono} \cdot \frac{1}{N} + r_{et} \cdot \frac{N-1}{N} \qquad (2.17)$$

where we used r_{mono}, which is commonly used in fluorscence anisotropy microscopy, instead of r_1 to denote the anisotropy arising from the initially excited molecule. So in fact (2.17) implies that the probability of emission is the same for all molecules in the cluster if we're considering steady state measurements with a high homo-FRET efficiency. Hence, the bigger the cluster the bigger the contributions from r_{et}, the depolarized anisotropy after energy transfer.

The effect of depolarization after energy transfer was first calculated by [1], assuming parallel transition dipole moments and a randomly oriented ground state distribution. If the fluorophores don't exhibit rotational diffusion, r_{mono} and r_{et} were found to be 0.4 and 0.016 respectively. Taking into account no perfectly aligned absorption and emission dipoles and little rotation of the probes left them with the conclusion that the fluorescence is completely depolarized after one single energy transfer event. However, it turns out that this assumption is not correct. Therefore, additional reference measurements on constructs of known cluster size, which can be verified using native PAGE analysis, need to be done in order to determine r_{et}[4]. A detailed description of native PAGE analysis will be given in chapter 3.

2.5 Polarization affecting factors

In fluorescence anisotropy experiments, it's all about quantitatively measuring the emission polarization in a proper manner. This implies that all processes affecting the polarization should be taken into account. In this section we will give an overview of the most common depolarization factors present in (wide-field) fluorescence microscopy. Besides that, photobleaching in is briefly discussed as it enhances the polarization in homo-FRET experiments.

2.5.1 High numerical aperture objectives

Anisotropy measurements are based on the photoselective excitation of fluorophores by polarized light. Fluorophores preferentially absorb photons whose electric field vectors are aligned parallel to the transition dipole moment of the fluorophore, as the probability of absorption is proportional to $\cos^2\theta$(see Appendix A), where θ is the angle the absorption dipole makes with the electric field vector of the excitation light[24]. Therefore, also fluorophores that are oriented slightly off-axis, with respect to the excitation polarization, are excited and hence the theoretical maximum anisotropy, r_0, upon one photon excitation is only 0.4.

However, in this derivation we assume the excitation and emission polarization are not affected by the objective, which is unfortunately not realistic. Due to the high numerical aperture, which is equivalent to a wide solid angle subtended by the objective, the observed polarization decreases, as will become clear in a moment.

If we define a set of right-handed coordinate axes such that the X_1-axis is parallel to the optical axis of the objective and the X_3-axis is parallel to the electric fieldvector of the polarized excitation light(See Appendix). Now consider an emission dipole in the sample has components (x_1, x_2, x_3) along these axes. The fluorescence polarization intensities by this single dipole are then given by[3]

$$I_\parallel = K_a x_1^2 + K_b x_2^2 + K_c x_3^2 \tag{2.18}$$

$$I_\perp = K_a x_1^2 + K_c x_2^2 + K_b x_3^2 \tag{2.19}$$

with

$$K_a = 1/3(2 - 3\cos\sigma + \cos^3\sigma) \tag{2.20}$$

$$K_b = 1/12(1 - 3\cos\sigma + 3\cos^2\sigma - \cos^3\sigma) \tag{2.21}$$

$$K_c = 1/4(5 - 3\cos\sigma - \cos^2\sigma - \cos^3\sigma) \tag{2.22}$$

where σ denotes the half angle subtended by the objective aperture as viewed from the sample. As well known, σ is related to the numerical aperture, NA, and the refractive index of the medium, n, via

$$NA = n\sin\sigma \tag{2.23}$$

The parallel and perpendicular intensities were solved and plotted as a function of the numerical aperture of the objective, as shown in figure 2.4. We see that the polarization for a $NA = 0.6$ objective is mainly preserved, as the drop in anisotropy is only about 4%. Though the decrease in polarization for a $NA = 1.2$ water immersion objective is more significant, as the anisotropy drops over 10% relative to the former low NA-objective.

This depolarizing effect of high numerical objectives should be taken into account in fluorescence anisotropy experiments. The choice for an objective is always a competition between resolution and sensitivity(higher numerical apertures collects more light) on one hand and
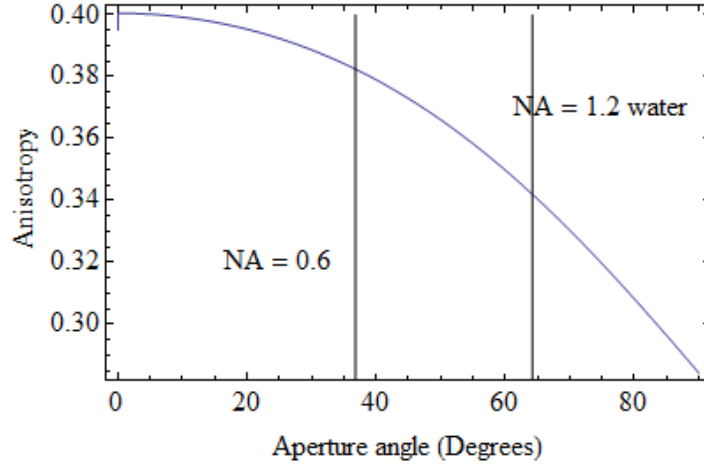
Figure 2.4: Depolarizing effect of high numerical aperture objectives. The theoretically found difference between a NA=0.6 and a NA=1.2(water immersion) objective is about 10%.

depolarization on the other. Seeking for more resolution is at the expense of preserving polarisation and vice versa. In general, using objectives with numerical apertures up to 0.75 significantly reduces the depolarizing effect[21].

2.5.2   Rotational diffusion

Rotational diffusion of fluorophores is the most common source of quenching the polarization and thus lowering the anisotropy. Such diffusion occurs during the lifetime of the excited state and thus it displaces the emission dipole of the fluorophore before emission. In fluid solution most fluorophores rotate extensively within 50 to 100 ps[23]. Hence the molecules can rotate many times during the 1-10 ns excited-state lifetime and the emission is depolarized. For this reason fluorophores in solution typically show anisotropies near zero. Assuming no other anisotropy-quenching processes to take place, the expected anisotropy as a function of the lifetime τ and rotational correlation time θ is given bij Perrin's equation[24]:

$$r = \frac{r_0}{1 + (\tau/\theta)} \tag{2.24}$$

where r_0 denotes the maximum anisotropy to be measured in the absence of rotational diffusion. So, only if $\tau \ll \theta$, i.e. the rotational diffusion during the lifetime of the excited state is very low, then the depolarizing effects of rotational diffusion are negligible.This requirement can easily be met by using big fluorophores(e.g. Green Fluorescence Protein(GFP), in a viscous solution(e.g. glycerol) since then the rotational diffusion is greatly suppressed.

2.5.3   Background

Obviously, any sources of background(dark current, stray light, autofluorescence) affect the ratio of the intensities and thus change the anisotropy. Therefore, these background factors should be handled very careful in order to eliminate their influence on the anisotropy. The effect of autofluorescence will be discussed later on in section 2.6.4, as this requires an even more delicate treatment.
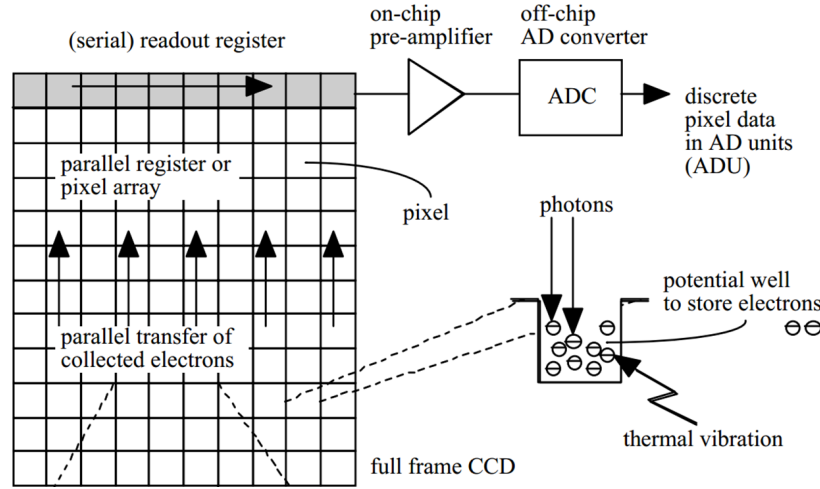
Figure 2.5: Schematic representation of a CMOS-camera. An absorbed photon creates an electron-hole pair. The electron is stored in a potential well, after which the electrons are transferred and the charge is amplified, which in turn is converted to ADUs.[39].

2.5.4   photobleaching

Besides the just mentioned depolarizing factors there's the effect of photobleaching in fluorescence microscopy that enhances the polarization upon homo-FRET experiments. If we are considering clusters of fluorophores exhibiting homo-FRET, the anisotropy generally goes down, as we've already seen. However, photobleaching effectively reduces the number of fluorophores in the multimer and hence photobleaching will lead to an increase of the anisotropy[25, 30]. Therefore photobleaching should be taken in mind when performing anisotropy measurements.

2.6   Accuracy of anisotropy measurements

In fluroscence anisotropy microscopy we're dealing with quantitative imaging and therefore the uncertainty in the eventually measured anisotropies are of great importance. The uncertainty is composed of several different components, which in some cases can be adjusted in order to increase the signal-to-noise ratio(SNR). In this section, we'll discuss all these sources of uncertainty relevant in fluorescence micsoscopy.

In our experiments, imaging was performed by high sensitive Andor Neo scientific Complementary Metal Oxide Semiconductor(sCMOS) camera's. In order to be able to understand the origin of the different sources of uncertainty, we need to have a detailed look on the operation of the sCMOS camera. An incident photon creates an electron-hole pair in the semiconductor layer of the chip. The electrons raised into the conduction band are collected in potential wells, where they stay for the specified integration time of the camera. After that, the charge stored in the potential wells is transferred(read out), amplified and converted into a discrete number(Analog Digital Units) on a pixel per pixel basis. In figure 2.5 the different steps of operation of a CMOS-camera are schematically shown.
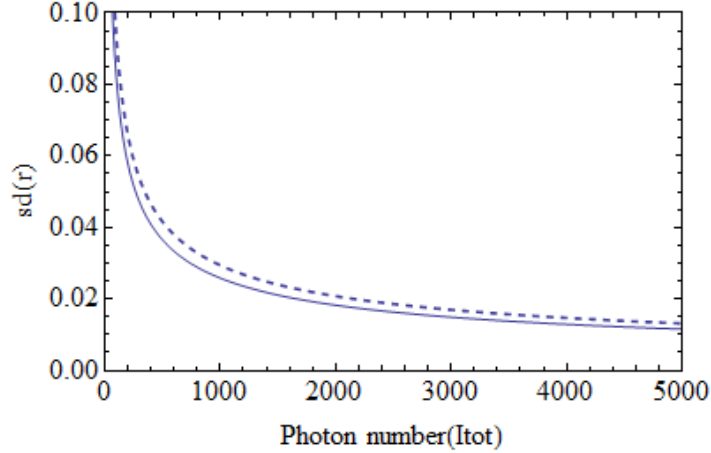
Figure 2.6: Dependency of the standard deviation of r on the number of photons I_{tot} detected for two cases: $r = 0$(straight line) and $r = 0.4$(dashed line). The higher the number of photons, the lower the uncertainty in the anisotropy.

2.6.1 Photon statistics

The actual output signal of the camera is given in ADUs, which is not equal to the number of photons detected since the charge contained by the potential wells is amplified before being converted into ADUs. As we are interested in the actually detected photons for our photon statistics, this gain factor is important.

The number of photons detected by the camera obeys Poisson statistics and therefore leads to a fundamental uncertainty in the measured anisotropy[7]. According to this Poisson statistics, the standard deviation σ of the number of photons is equal to the square root of the expected value. If we now assume that the G-factor can be determined with arbitrary accuracy, so the variance of G equals zero, and we apply standard propagation of uncertainty to (2.3) for uncorrelated signals we obtain the following expression for the variance in the anisotropy r [26]

$$v(r) = \frac{(1-r)(1+2r)(1-r+G(1+2r))}{3I_{tot}} \tag{2.25}$$

where $I_{tot} = I_{\parallel} + 2GI_{\perp}$ is the total emission intensity. Notice that the variance, and so the standard deviation $sd(r) = \sqrt{v(r)}$ as well, not only depends on the total number of photons(I_{tot}) but also on the value of r. The dependence of the uncertainty of r on the total number of detected photons is plotted in the figure for completely depolarized emission($r = 0$) and for the maximum anisotropy in case of one photon excitation($r = 0.4$).
In conclusion, there's a fundamental limit to the accuracy of the determination of the anisotropy due to the quantum nature of light.

2.6.2 Thermal noise

Without being exposed to any photons, there are still electron-hole pairs created in the semiconductor layer due to thermal vibration, leading to thermal noise or so-called dark

current. Again, the generation of these photo-electrons is governed by Poisson statistics, but more importantly, the production rate is an increasing function of temperature[39]]. As a consequence, the dark current is greatly reduced by cooling of the semiconductor chip, down to -40° C.

Furthermore, impurities in the semiconductor layer of the chip can cause hot pixels, which extremely suffer from dark current. The dark current of these pixels can also be adequately suppressed by cooling of the chip.

2.6.3 Readout noise

Let's briefly recall the order of operation of the camera: (1) electrons are transferred to the amplifier (2) where the voltage induced by the charge is amplified and measured (3) after which the voltage is converted into discrete numbers yielding the pixel value. The readout noise mainly arises in step (2) as the amplifier doesn't do a perfect job in measuring the charge of the electrons. The uncertainty in this measurement determines the readout noise, which is usually given in electrons as the charge is obviously made up of electrons.

For low readout rate the noise is minimal and about constant. However, for high readout rates the noise increases and becomes a significant component of the total noise[39]. The readout noise only depends on the readout rate, not on exposure time or photon flux.

2.6.4 Autofluorescence

As mentioned before, autofluorescence of cells influences the anisotropy and so needs to be treated carefully. The autofluorescence of the cell does not necessarily need to be evenly polarized as the fluorescence signal itself and therefore the anisotropy could change upon subtraction upon the actual measured autofluorescence value. Let's try to get any numbers for the amount of change to be expected due to differently polarized autofluorescence. Therefore, we recall (2.3), leaving G out of consideration and introducing contributions of autofluorence for parallel and perpendicular polarizations, A and B respectively, we find

$$r = \frac{(I_\parallel - A) - (I_\perp - B)}{(I_\parallel - A) + 2(I_\perp - B)} \tag{2.26}$$

Let's now see what happens if we take a certain anisotropy, say $r = 0.25$, for which we find intensities of $I_\parallel = 3000$ and $I_\perp = 1500$ without correction for autofluorescence. Furthermore, we assume the parallel autofluorescence to be 10% of the parallel intensity, so a value of 300. We can now plot the anisotropy for these numbers for values of the perpendicular autofluorescence, as depicted in figure 2.7. If the autofluorescence is evenly polarized as the fluorescence signals, then the perpendicular intensity of the autofluorescence is 10% as well, corresponding to 150. The other limit would be totally depolarized autofluorescence, for which the net contributions of both signals would be equal, i.e. perpendicular intensity is 300 too. The graph clearly shows an increase in anisotropy if the autofluorescence is depolarized with respect to the fluorescence signal, up to 17% in case of totally depolarized autofluorescence.
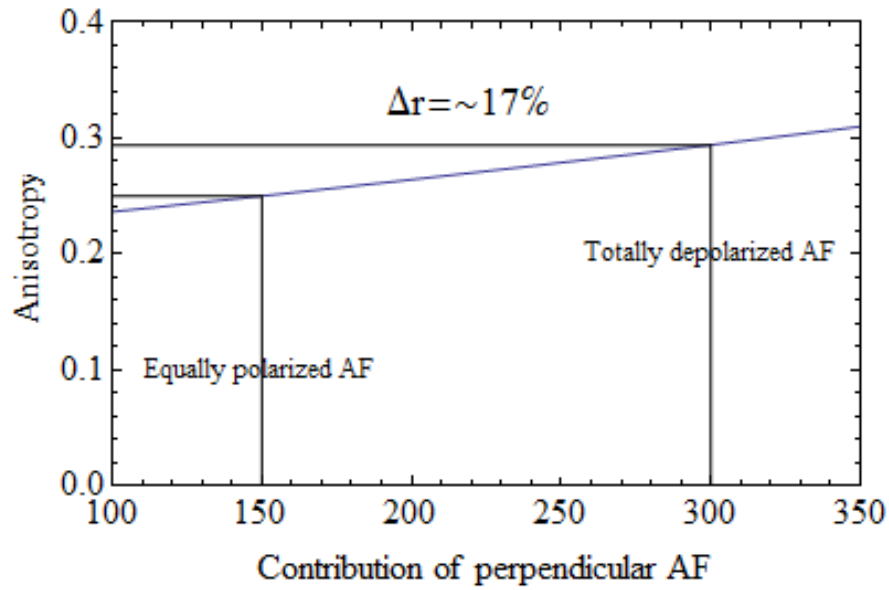
Figure 2.7: Dependency of the anisotropy on the contribution of autofluorescence for a $I_{\parallel} = 3000$ and $I_{\perp} = 1500$ and hence $r = 0.25$. The autofluorescence was taken to be 10% for $I_{\parallel}$, so 300, while the AF of $I_{\perp}$ was varied. The difference between AF being as polarized as the signal and AF being totally unpolarized is roughly 17%.

Chapter 3

Materials and Methods

Fluorescence anisotropy measurements can be performed on a wide range of available imaging modalities in order to detect homo-FRET. Wide-field, confocal one photon and multiphoton as well as TIRF(evanescent field imaging) microscopy are all suitable imaging methods for measuring fluorescence anisotropy with high resolution. In principle, those imaging modalities all involve excitation of the sample with polarized light and detection of the emission polarization which determines the anisotropy. However, the experimental arrangement and practical considerations of the mentioned techniques differ greatly due to their varying characteristics. In this chapter we will describe our design and practical considerations for setting up a wide-field fluorescence microscope for simultaneous detection of the polarized emission components.

3.1 Imaging setup

In our wide-field fluorescence anisotropy measurements we used a Nikon Ti epsilon microscope body that can be adjusted to almost any desired configuration in terms of optics. As mentioned above, simultaneous detection of the polarized emission components is required and therefore we used a design, as shown in figure 3.1, in which the parallel and perpendicular intensities are split.

3.1.1 Excitation

The microscope body was equipped with a short-arc mercury lamp, which is widely used in wide-field fluorescence microsopy because of its brightness and its broad emission spectrum, ranging from the uv-light to the infrared. Therefore, mercury lamps are suitable as an excitation source for all kinds of dyes. After passing some neutral density filters, a heat shield and an IR-filter(which enables the operation of the perfect focusing system of the microscope), the light enters an ultra broadband wire grid polarizer(Thorlabs, WP25L-UB) that has a transmission of roughly 70% and an extinction ratio over 5000 for our excitation spectrum. Especially the extinction ratio is of great importance as a high quality excitation polarization is needed in order to get a well defined excited state population. A bandpass filter(460-500 nm) was used to select the excitation wavelength after which the light strikes a dichroic mirror(505 nm) and approaches the objective(Nikon S Plan Fluor, NA=0.6/40x air, wd 2.8-3.6) where the light is focused into the sample. The objective should be chosen properly, since
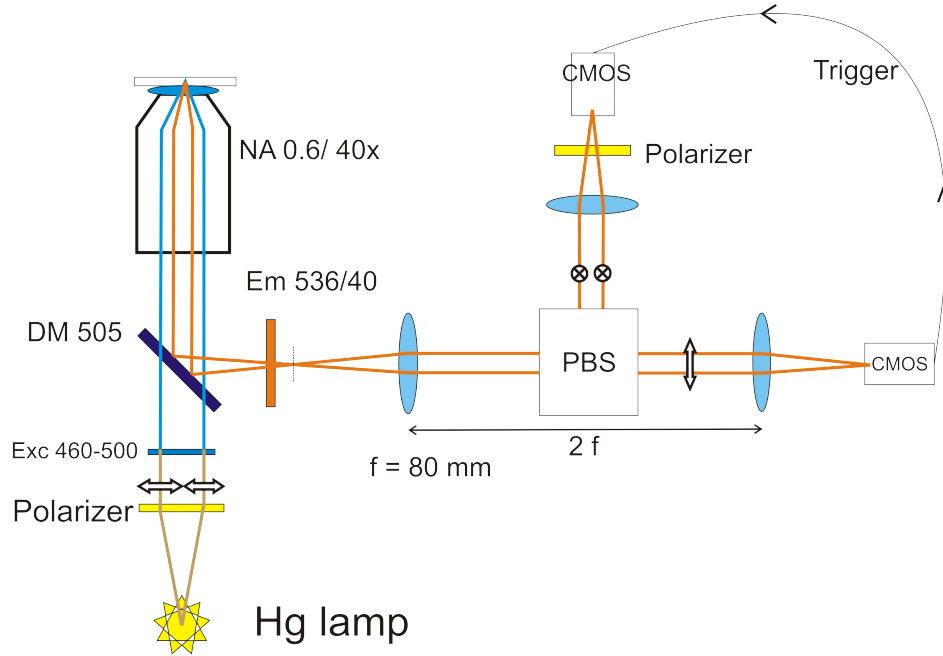
Figure 3.1: Schematic overview of the experimental setup for simultaneous detection of the emission polarizations.

high NA objectives do enhance the resolution but depolarize the excitation polarization, as was discussed in detail in chapter2.

3.1.2 Emission path

As in the case of any fluorescence microscope, fluorescence emission, after being collected by the objective, is selected for the specific wavelength bandwidth by the dichroic mirror and a band pass filter(536/40 nm). The beam is then collimated by a f=80 mm achromatic doublet lense(Thorlabs, AC-508-080-A-ML). The orthogonal polarization directions are split by a polarizing beam splitter(Thorlabs, CM1-PBS-251), where the light is transmitted and reflected for parallel and perpendicular oriented electric field vectors respectively. Here, the orientations are defined with respect to the direction of the excitation polarization. The same f=80 mm achromatic lenses were used in each detection path to focus the beam onto two Andor Neo sCMOS cameras, which are connected to each other such that one can trigger the other in order to take images simultaneously(the delay due to the trigger was measured to be less than 10 μs, very small compared to the exposure time). The extinction ratio of the polarizing beamsplitter for the transmitted beam is about 1000, which is high enough. However, the extinction ratio of the reflected beam is only 30-40(see specs beamsplitter). Therefore, we mounted a wire grid polarizer(Thorlabs, WP25M-VIS, ER: 600) in the detection path of the reflected beam in order to enhance the extinction ratio.

Furthermore, the whole detection system forms a closed circuit in terms of stray light contamination. Besides that, all tube lengths between beamsplitter and microscope and between beamsplitter and cameras can be adjusted to facilitate the alignment process.
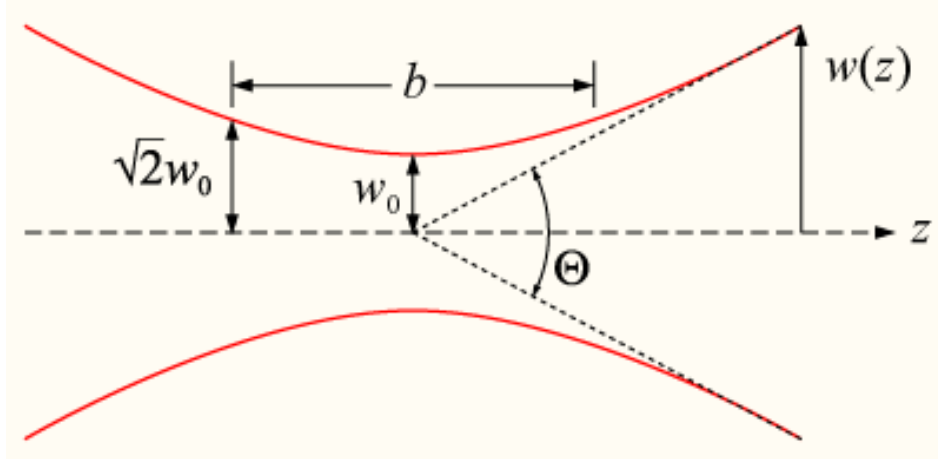
Figure 3.2: Gaussian beam representation of the depth of focus. Due to the fact that the beam converges to the focal point and diverges again afterwards, the focal plane is finite in the z-direction and hence the depth of focus b is approximately 200 nm in our experimental arrangement.

3.1.3 Alignment

The alignment process is a challenging task and cannot be underestimated as it's very important. Since we image the same object in two different detection channels, both channels need to be aligned very accurately. As we just mentioned, we can collimate the beam towards the beamsplitter by adjusting the tube length between micsoscope and beamsplitter. In the same way we can adjust the tube length between beamsplitter and cameras to look for the best focus on the cameras. The beamsplitter itself can be tilted and rotated quiet sensitive in order to align both objects on the cameras.

How critical the alignment of the distance of the cameras to the beamsplitter is, becomes clear when we consider the depth of focus(DOF) of the beams. Assuming Gaussian beam optics(as depicted in figure 3.2) , we can express the spot size as a function of the distance, z, from the focus as

$$w(z) = w_0 \sqrt{1 + (\frac{z}{z_R})^2} \tag{3.1}$$

where w_0 is the beam waist, z_R is the Rayleigh range,the distance along the propagation direction of a beam from the waist to the place where the area of the cross section is doubled[33]. This Rayleigh range is given in terms of the wavelength and the beam waist

$$z_R = \frac{\pi w_0^2}{\lambda} \tag{3.2}$$

The DOF, b, is now defined as twice the Rayleigh range, the point where the beam width is $\sqrt{2}$ times the beam waist:

$$b = 2z_R = \frac{2\pi w_0^2}{\lambda} \tag{3.3}$$

Now, w_0 is diffraction limited, taking into account a 40x objective, yielding a beam waist of 4μm for green light. Substitution in (3.3) gives

$$b = DOF = \frac{2\pi w_0^2}{\lambda} \approx 200\mu m \tag{3.4}$$

So, we see that the DOF is only 200 μm and hence the alignment is very critical.

3.2   Calibration of the setup

Obviously, the calibration of the setup is important. As discussed in chapter 2, several aspects of the microscope setup limit the dynamic range of the measurable anisotropy. The measurements required to account for these effects will be discussed in this section.

3.2.1   G-factor measurements

One of the measurements to be done is the determination of the G-factor. If we expect unpolarized emission from a certain sample, we'd expect equal intensities for both the parallel and perpendicular channel in an ideal setup. However, we're dealing with a lot of optics that could possibly change the polarization to a some extend. For example, reflections from mirrors are more polarized in the direction perpendicular to the incident plane of the light than the incident beam itself. The Brewster angle is the ultimate example, where the reflected light is even perfectly polarized.
As the optics in the setup exhibit these kind of preferential polarization effects, you have to compensate for that. Usually this is done by measuring the emission from a solution of a small dye. Here we used fluorescein in water. Fluorescein is a rather small molecule that rapidly spins around its axis in a low-viscous buffer like water. Thus, the rotational diffusion during the lifetime of the excited state is very high and so the emission is completely depolarized. If the emission is then measured in terms of both polarizations, the polarizing off-set of the setup is given by $G = I_\parallel / I_\perp$.

3.2.2   Reference measurements on GFP

As was briefly discussed in section 2.5.2, the maximum anisotropy is found when the involved fluorophores exhibit no rotational diffusion during their excited state lifetime, assuming no other depolarizing effects as described in section 2.5. Since GFP is a large molecule, with parallel absorption and emission dipole moments, and glycerol is a viscous buffer, GFP in glycerol/water solution is widely used as a reference measurement for the maximum anisotropy achievable on a certain setup configuration. It has been pointed out that GFP in solution at high concentration has the tendency to form twofold symmetric dimers[20, 40]. The dissociation constant of GFP have been determined to be approximately 100 μM[29, 42]. Therefore, high GFP concentration should be avoided in order to obtain a representative reference value.
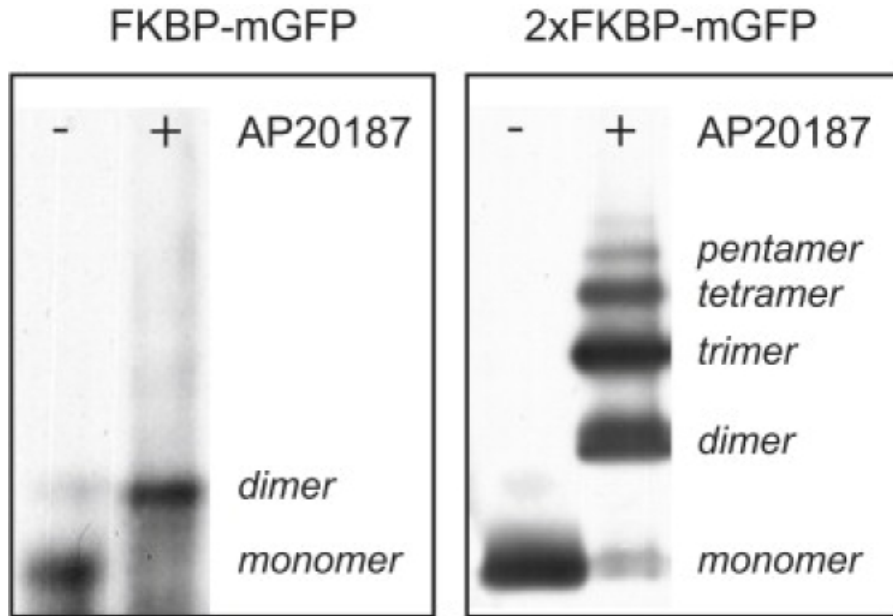
Figure 3.3: Native PAGE analysis of dimerization constructs of cells expressing FKBP-mGFP or 2xFKBP-mGFP. Both single and double FKBP constructs form monomers in the absence of AP20187 but dimers and oligomers respectively when its ligand AP20187 is added. [4]

3.3 Biological samples

3.3.1 Fluorophore choice for homo-FRET

One of the requirements for homo-FRET is spectral overlap between the absorption and emission spectra of the fluorophore. Besides that, the fluorophore must have a nonzero initial anisotropy, so no complete depolarization due to rotational diffusion during the lifetime.Moreover, the fluorophore needs to be photostable in its environment. Thus, the choice of fluorophore and the method of tagging to the specific protein or molecule of interest is very important.
GFP is a genetically encoded fluorescent protein that meets all these requirements and was succesfully used for homo-FRET measurements in the past[2, 4]. Therefore, in this study GFP was used for labelling.

3.3.2 reference constructs

In section 2.4.3 we discussed the reason why we need to perform reference measurements on samples of known cluster size. In this study, FKBP-mGFP and 2xFKBP-mGFP constructs are used, which form monomers in the absence of AP20187 but dimers and oligomers respectively when AP20187 is added, as shown in the native PAGE analysis in figure 3.3.

Relative depolarization, as shown in figure 4.1, values due to clustering, r/r_{mono}, of the reference constructs were determined via confocal fluorescence microscopy by Bader et al.. The value of r/r_{mono} was found to be 0.81 for dimers and 0.72 for oligomers.
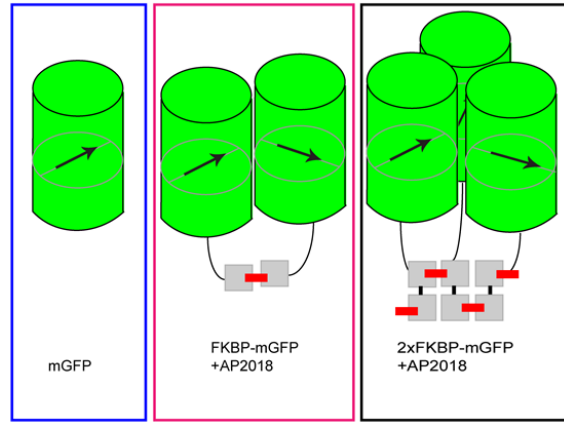
Figure 3.4: Model for the clustering of single and double FKBP-mGFP constructs upon addition of AP20187, showing their dimerization and oligomerization respectively.

3.3.3   EGFR samples

Besides the reference constructs, clustering of labelled EGFR receptors was investigated. Again, when adding a binding ligand like AP20187, EGFR-FKBP-mGFP can form dimers and EGFR-2xFKBP-mGFP can form oligomers, in analogy with the reference constructs. This process is depicted in figure 3.5. The same clustering effect is to be expected for EGFR bound to EGF, so these constructs were studied as well.

3.4   Protocol for anisotropy imaging measurements

Doing quantitative imaging on our wide-field setup requires extreme handling precision. Some key parameters need to be determined very accurate each time a mesurement is done since there can be slight changes in alignment and changes of the microscope settings for seperate experiments. Obviously, for instance all reference measurements need to be performed with the same setup settings as the settings for the actual experiments. Therefore, a protocol for performing anisotropy mesurements will be presented in this section in order to ensure that all steps are taken in the right sequence. In this way the experiments will always be done in the same manner, yielding most reliable and reproducable results.

Before starting a measurement series, the mercury lamp needs to be aligned according to the so-called Köhler illumination. Besides that, using a coverplate on top of the sample to reduce stray light is highly recommended. Moreover, Increasing the intergration time increases the SNR, but mind the effect of photobleaching.

- **Imaging of beads**

  As we will discuss in section 3.5, the process of image registration is a crucial one in obtaining high quality results. The first step in this process consists of taking images in order to facilitate the image registration. The process in MATLAB involves intensity
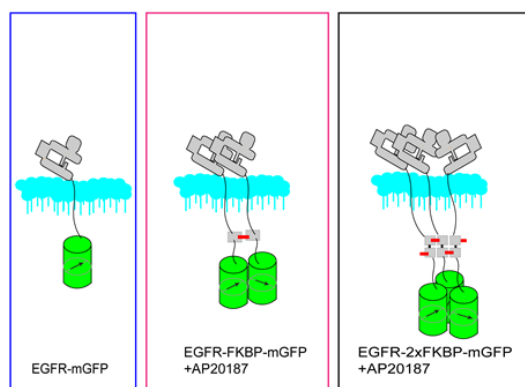
Figure 3.5: Model for EGFR-FKBP-mGFP clustering in the presence of AP20187, where the blue part represents the cell membrane with the epidermal growth factor receptor on top. Clearly, measuring homo-FRET between the GFP molecules is equivalent to detecting clustering of the EGF receptors.

based registration and so we use fluorescent, 200 nm in diameter, beads illuminated with unpolarized light to ensure totally depolarized emission, yielding almost equal images for both polarizations in terms of intensity. Moreover, the beads are spherical objects creating a nicely defined point spread function which facilitates the registration process even more.

When the images are acquired, ensure that the excitation polarizer has been taken out and be careful there are no beads situated at the edge of the selected region of interestes. Also, make sure both images contain the same beads so all beads are present in both the p- and s-image. If these requirements are not met, the chance the registration process fails, increases significantly.

- **Determination of G-factor**

  The G-factor is measured by using highly rotational diffusing fluorophores. For instance fluorescein in an aqauous solution. Although the rotational diffusion during the fluorescence lifetime should be high enough, totally depolarized emission is guaranteed by using unpolarized excitation light. Furthermore, the objective must be focused right in the middle of the sample since the molecules near the coverslip could be stuck to the glass. Therefore, use the diaphragm of the microscope body to select a proper focal plane.

  In this way, a G-factor image is obtained that is pixel dependent, i.e. the G-factor is not a number but varies over the chip. Keep in mind that a rather high integration time, typically 10 s, increases the signal-to-noise ratio.

- **GFP reference measurement**

  Each time a measurement will be done, the maximum anisotropy could change. Using another objective, for instance, affects the excited state population and hence influences

the maximum anisotropy, which serves as a reference value. GFP in a viscous solution like glycerol hardly exhibits rotational diffusion during the fluorescence lifetime and is therefore widely used as a reference sample in fluorescence microscopy[4].

In order to avoid dimerization of the GFP monomers, low concentrations, typically in the order of μM, of GFP should be used. Too low concentrations should be avoided as well since this is of the cost of intensity and hence of the SNR. Of course, polarized excitation is required and again be sure to focus right in the middle of the sample.

- **Cell selection**

  In the actual experiment, one needs representative cells. Therefore it's important to select cells suitable for imaging. Both over- and under-expressing cells should be avoided. Depending on the sample in question to be measured, the interesting parts of the cell differ. For instance, when measuring GFP linked to EGFR, the cell membrane must be in focus. Per sample, it's recommended to image multiple different cells as this increases the statistics.

- **Imaging of autofluorescent cells**

  As we already discussed and quantified in the theory, the contribution of autofluorescence to the emission is significant and therefore cannot be neglected in the data analysis process as it affects the measured anisotropy(see section 2.6.4). Therefore, measuring unlabelled cells provides a quantification of the autofluorescence of the cells. Since also the solution in which the cells are embedded could possibly affect the emission, untransfected cells prepared in the same way as the other samples must be used. Furthermore, the microscope and camera settings need to be equal to those used in the actual experiments.

3.5 Data analysis

Data analysis has proven to be one of the main challenges in our wide-field microscopy setup. There are several key factors that appear to be of great significance in obtaining reliable and reproducable results. In this section we will discuss among others the processes of image registration, determination of background autofluorescence and...

3.5.1 Image registration

The anisotropy data were obtained by using two detection paths, seperated channels for each polarization as described in chapter Materials and Methods. Although the setup was aligned very accurately, the alignment is not perfect. The pixel size of the Andor cMOS Neo cameras is $6.5 \times 6.5 \mu m$, which means that both cameras need to be aligned with an accuracy of the same order to get a proper alignment. Besides that, we've got some optics(polarizing beamsplitter, achromatic lense and wire grid polarizer) that deviate the beams which obviously complicate the alignment process.

Analysis of the acquired images involves pixel by pixel comparison of the intensity. However, if the images are slightly transformed with respect to each other, a pixel of one image doesn't

correspond to the same pixel on the other image. So in order to be able to do quantitative analysis of the images, registration of the images is required.

Image registration has been subject to research for many years[18, 43] and has also been applied in fluorescence microscopy[9–11, 22, 41]. Image registration is the process of overlaying images of the same scene taken by different sensors. In this process the *moving* image is geometrically aligned with the *fixed* image. In our data analysis process, the registration of images is a crucial step since we compare intensities of the parallel and perpendicular emission on a pixel scale.

In fact, registration can be seen as the optimization of a similarity metric over all kinds of transformations. There are three necessary aspects to be defined for image registration: a transformation model, a similarity metric and an optimization method[15]. The actual choices for these aspects depend on the desired accuracy of the registration outcome.

Transformation matrix

Depending on the nature of the geometric distortion we can indicate different types of transformation models. In our case it's sufficient to use an affine transformation, which covers translation, rotation, scaling and shear and so we'll take this transformation model as an example. The relationship between the geometric parameters $\alpha = t_x, t_y, \theta, s_x, s_y, k$ and the transformation parameters $a = [a_1, a_2, a_3, a_4, a_5, a_6]^T$, as well as the individual transform matrices are given by[15]

$$A_\alpha = \underbrace{\begin{bmatrix} 1 & 0 & t_x \\ 0 & 1 & t_y \\ 0 & 0 & 1 \end{bmatrix}}_{translation} \cdot \underbrace{\begin{bmatrix} \theta_c & -\theta_s & 0 \\ \theta_s & \theta_c & 0 \\ 0 & 0 & 1 \end{bmatrix}}_{rotation} \cdot \underbrace{\begin{bmatrix} 1 & k & 0 \\ 0 & 1 & 0 \\ 0 & 0 & 1 \end{bmatrix}}_{shear} \cdot \underbrace{\begin{bmatrix} s_x & 0 & 0 \\ 0 & s_y & 0 \\ 0 & 0 & 1 \end{bmatrix}}_{scaling} = \begin{bmatrix} s_x\theta_c & s_y(k\theta_c - \theta_s) & t_x \\ s_x\theta_s & s_y(k\theta_s + \theta_c) & t_y \\ 0 & 0 & 1 \end{bmatrix} = \begin{bmatrix} a_1 & a_2 & a_3 \\ a_4 & a_5 & a_6 \\ 0 & 0 & 1 \end{bmatrix}$$

$$(3.5)$$

where the geometric parameters in α denote the following
t_x = translation in the x-direction
t_y = translation in the y-direction
θ = angle of rotation, with $\theta_c = \cos\theta$ and $\theta_s = \sin\theta$
k = shear factor along the x-axis
s_x = scale factor in the x-direction
s_y = scale factor in the y-direction

Note that the above affine transformation matrix corresponds to a transformation with respect to the center pixel. As the command *imregtform* in the MATLAB script we use for the determination of the transformation matrix specify a transformation with respect to the top-left pixel[15], we can rewrite the transformation matrix accordingly, yielding[15]

$$\begin{bmatrix} s_y(\theta_c + k\theta_s) & s_x\theta_s & 0 \\ s_y(k\theta_c - \theta_s) & s_x\theta_c & 0 \\ t_x + x_c - s_yx_c(\theta_c + k\theta_s) + s_yy_c(\theta_s - k\theta_c) & t_y + y_c - s_x\theta_sx_c - s_x\theta_cy_c & 1 \end{bmatrix} = \begin{bmatrix} t_1 & t_4 & 0 \\ t_2 & t_5 & 0 \\ t_3 & t_6 & 1 \end{bmatrix}$$

$$(3.6)$$

So, if we know the total transformation matrix in terms of t_i we can identify the four different types of geometric transformations as we got six unknown parameters and six equations, from which it follows that

$$s_x = \frac{t_5}{\cos\theta} \tag{3.7}$$

$$s_y = \frac{t_1}{\theta_c + k\theta_s} \tag{3.8}$$

$$\theta = \arctan\frac{t_4}{t_5} \tag{3.9}$$

$$k = \frac{t_2\theta_c + t_1\theta_s}{t_1\theta_c - t_2\theta_s} \tag{3.10}$$

$$t_x = t_3 + \frac{N}{2}(s_y(\theta_c + k\theta_s) - 1) - \frac{M}{2}s_y(\theta_s - k\theta_c) \tag{3.11}$$

$$t_y = t_6 + \frac{M}{2}(s_x\theta_c - 1) + \frac{N}{2}s_x\theta_s \tag{3.12}$$

where [M,N] denotes the size of the transformed image in pixels.

Image registration in MATLAB

As mentioned before, the images are taken with Andor Solis for Imaging and background was subtracted in ImageJ. After this step, all further analysis was done in MATLAB. The whole procedure from registration of images till the final calculations of the anisotropy, if necessary with a selected region of interest, was done using MATLAB-scripts.

A registration process requires three aspects. The transformation model, as described in section 3.5.1, is needed to point out the different types of distortions for the transformation function. The similarity *metric* is an object that defines a quantitative measure for the similarity between the images. T his similarity has to be optimized in order to get the best registration. Therefore, an *optimizer* method must be selected to search for a set of transformation parameters which optimally aligns the two images according to the given similarity metric.

The *metric* used in MATLAB is a *Mutual Information* metric which is a measure of statistical dependency between the two data sets(the images) and it is particularly suitable for registration of images from different modalities[43]. To be more specific, MI maximizes the number of coincident pixels with the same relative intensity. For that reason, the registration method is called 'intensity-based'. The optimizer is an object that specifies the way of maximizing the amount of mutual information, i.e. maximizing the similarity between the images. Optimization methods typically converge to local extrema, therefore initial estimates or initial approximate alignment are necessary[15]. Practically this means that the default optimization settings in MATLAB sometimes need to be adjusted in order to get an optimal registration. For instance, increasing the maximum number of iterations or decreasing the minimum step length of the optimization process could enhance the accuracy of the registration.

3.5.2 Determination of autofluorescence

The contribution of autofluorescence to the emission is significant and therefore cannot be neglected in the data analysis process as it affects the measured anisotropy(see section 2.6.4). The problem that arises is the fact that the emission from autofluorescence is not distinguishable from the fluorescence signal. This means that the autofluorescence needs to be determined in an alternative way, after which the actual measured intensities can be adjusted for.

The solution is measuring unlabelled cells under the same circumstances as under which the experiments were done. As was described in section(samples..), the cells express GFP due to the fact that they are transfected such that their DNA encodes for GFP. Since autofluorescence includes emission from all biological structures in the cell other than GFP, the emission from untransfected cells will contain only autofluorescence. Therefore, measuring these untreated cells provides a quantification of the autofluorescence of the cells.

3.5.3 Protocol for data analysis of samples

In section 3.4, a protocol was provided for the imaging part of the measurements. However, we're not only interested in the imaging part so in this section a protocol will be provided for the data analysis process. The majority of our data analysis was performed in MATLAB and only a little in ImageJ. All steps, from the unregistered, raw images to the final anisotropy data, will be treated in detail in this section.

- **Subtracting background**

  The importance of background correction for autofluorescence was already pointed out but here we describe its quantification and the subtraction procedure.

  In principle, the autofluorescence differs per part of the cell. Therefore, the autofluorescence must be determined for those regions that we are interested in, avoiding for instance the Golgi-apparatus, nuclei and mitochondria as they can exhibit significant higher or lower autofluorescence. Typically, there's a rather high variation in the autofluorescence so its value can obnly be estimated with a relatively high uncertainty.

  This background value is then subtracted from the raw data in ImageJ. This procedure needs to be performed for both polarizations, as the autofluorescence can be polarized as well. The ImageJ macro for background subtraction can be found in Appendix B.

- **Calculation of transformation**

  Before being able to register the images, we need to determine the transformation between them for which we took the fluorescent beads images. We wrote a script in MATLAB to calculate the transformation. The only input arguments are the two images, which are registered for any affine transformations(see section 3.5.1 for more details). The output argument is the transformation matrix, which can be decomposed into the four different geometric transformations involved in an affine transformation according to (3.6). In fact, the composition of this transformation matrix is not that important, since we only use the transformation matrix itself. However, it's recommended to keep an eye on the value of the translation between the images as this is a number that can be easily verified by having a look at the raw images. In this way, a possible failure

in the registration can be quickly noticed. For details about the MATLAB script, see Appendix B.

- **Determination of G-factor**

  The G-factor is a measure for the difference in sensitivity of both detection channels(see section 3.2.1), i.e. the ratio of $I_\parallel$ and $I_\perp$. Obviously, the s-polarized image needs to be transformed according to the transformation matrix we just found, before calculating the G-factor image. Again we emphasize that G is an image, so pixel dependent, not a fixed number. The MATLAB script requires the two images and the transformation as input, while returning the G-factor output image. The MATLAB script is included in Appendix B.

- **Threshold setting**

  In chapter 2 we already pointed out that photon statistics limits the uncertainty in the anisotropy. This is a reason why we want to get rid of low-intensity pixels. Besides that, in the raw images some sort of halo can be distinguished around the cell where the intensity builds up, which can be considered as the result of the convolution between the optical transfer function(OTF) and the cell. Since we are interested in the membrane in certain cases, we would like to determine the exact place of the membrane, ignoring this halo-effect. For these reasons we can set a threshold on one of the raw images, for example the parallel image. The treshold can be determined best by plotting a lateral profile of the raw parallel image in ImageJ and determining the 'begin' of the cell by taking the pixel value corresponding with half the change in intensity, i.e. at the point where the 'build up' of intensity is 50% of the value where the intensity levels off.

- **Calculation of anisotropy**

  Now, the pre work has been done. We determined the transformation, registered the images, calculated the G-factor and set the threshold. If we recall equation (2.3) from chapter 2, we've got all the information we need to perform the actual anisotropy calculations. Again, a MATLAB script was written to do so. In principle, four input arguments are required: the parallel and perpendicular image, the transformation matrix and the G-factor. The script will then return the anisotropy image for all pixels(including low-intensity pixels), the average anisotropy over all pixels values above the threshold, the anisotropy image from pixels above the threshold, the registered perpendicular image and the parallel image. The multiple output arguments, which of course can be adjusted, enable you to easily verify things, e.g. the registered perpendicular image and the input parallel image can be overlaid to check the registration process. The corresponding MATLAB script can be found in Appendix B.

- **Region of interest selection**

  The script returns the anisotropy of all parts of the image that exceed the threshold we set on the parallel polarization image. Since we are not interested in the average anisotropy of the whole cell, we can select a region of interest(ROI). Depending on the sample in question, we can for instance be interested in the cytoplasm or the cell membrane. These regions can be easily selected manually in a greyscale image of the anisotropy obtained in the previous step. After that, the average anisotropy of the designated ROI will be provided by the script.

Chapter 4

Results

All measurements were performed according to the protocol described in section 3.4. We selected a region of interest on the chip of 500 x 500 pixels, as we don't need the whole chip for measuring single cells. Since the images of the default settings of the cameras are mirrored, with respect to each other, in the vertical center axis of the chip, the imaging software(Andor Solis for Imaging 4.22.30007) needs to flip the image of the second camera. This flipping function can only be used around the center axis, so therefore the ROI was chosen around the center of the chip. Furthermore, all images were acquired with an exposure time of 10 seconds, which significantly increases the signal to noise ratio.

4.1 Calibration measurements

The calibration measurements were performed as discussed in section 3.2.

4.1.1 G-factor

The G-factor images show quiet high intensities, in the order of 10000 counts per pixel. Therefore, the-signal-to noise ratio is enhanced and the uncertainty in its value decreased. A noise band of about 100 is observed, so roughly 1% of the signal. As we emphasized before, the G-factor is not a number but an image, i.e. its value varies per pixel and cannot be taken as the average of all the pixels of the ROI as the sensitivity may be pixel dependent. The value of G was measured to range from 1.27 to 1.34, which means that the detection sensitivity of our setup is higher for the parallel polarization than for the perpendicular polarization.

4.1.2 GFP in glycerol

We determined the, in principle, maximum anisotropy of the setup by imaging GFP in glycerol for several concentrations of GFP in order to judge its validity, as too high concentrations of GFP could cause dimerization(see section 3.2). Concentrations of $3, 7$ μM, $1, 85$ μM and $0, 37$ μM were measured. Due to too little signal from the lowest concentrations, we could only determine the anisotropy for the first two concentrations, yielding values of 0.291 and 0,297 respectively. Analysis of the GFP samples in a confocal microscope pointed out that the GFP molecules were stuck to the coverslip and therefore these measurements cannot be considered reliable.

4.2 Reference measurements

We performed the reference measurements on 2xFKBP-mGFP constructs with and without the addition of the binding ligand AP-20187, which causes clustering of the FKBP linkers. Five cells per sample were selected, avoiding both under- and overexpressing cells. The anisotropy was calculated for two different values of the autofluorescence, as the autofluorescence has a quiet high uncertainty: for parallel/perpendicular intensity values of (1) 210/150 and (2) 300/200. One measurement of an 2xFKBP-mGFP construct with low-intensity and therefore non-reliability was left out. Also a measurement of a 2xFKBP-mGFP construct with AP added was left out, since the nucleus of the cell is very bright, whereas addition of AP causes the FKBP-constructs to be pulled out of the nucleus, as is the case in all other cells. So probably, the AP didn't work well in that particular cell.

The threshold anisotropy images, obtained after setting the threshold for each cell, for case (1) are shown in figure 4.1 and 4.2. The anisotropy is displayed on a pixel per pixel basis and so we expect a varying value per pixel that obeys photon statistics. The anisotropy is quiet smooth over both cells, in accordance with this fundamental uncertainty. The scale of both images is the same, so we immediately notice the sample with addition of AP shows a decrease in anisotropy. Furthermore, we selected a region of interest, mainly avoiding the nucleus of the cell because of its deviating autofluorescence signal, and calculated the average anisotropy value. The anisotropy was measured for all cells and the averages of both samples were compared, as shown in figure 4.5. For the constructs without and with addition of the ligand AP-20187 we found anisotropy values of $0,339$ and $0,3165$, respectively. Therefore, the decrease in anisotropy for the 2xFKBP-mGFP constructs with AP added compared to the samples without AP, was found to be $6,5 \pm 1,2\%$. The anisotropies for the individual cells and their uncertainty are displayed in 4.3.

Threshold anisotropy images of the same cells, one for each sample, for case (2), so with subtraction of a higher autofluorescence value, are displayed in 4.6 and 4.7. Again, the anisotropy image is quiet smooth and clearly the sample with addition of AP20187 shows a lower anisotropy. The average anisotropy of the designated ROIs was determined and averaged over all cells per sample, yielding values of $0,346$ and $0,323$ for constructs without and with addition of its binding ligand. The difference in average anisotropy of both samples is given in figure 4.8, which shows a decrease in anisotropy of $6,7 \pm 1,2\%$ for the sample with AP-20187 added, so a slightly higher anisotropy difference than for the former background subtraction. Furthermore, we see that all individual cells show an increase in anisotropy after subtraction of a higher value of the autofluorescence. Besides that, the relatively low intensity cells show a bigger increase in anisotropy after subtraction of a higher autofluorescence number than the high intensity cells.

4.2.1 Effect of pixel binning

In early experiments, we employed the on-chip binning(2 x 2 pixels) function of the camera since the registration process wasn't yet optimized. Therefore, obviously the resolution of the images goes down, as the intensity of the four pixels in the 2x2-array is summed to and taken as just one pixel. The registration procedure involves intensity-based comparison of both images and hence the quality of the registration will diminish upon pixel binning due to this
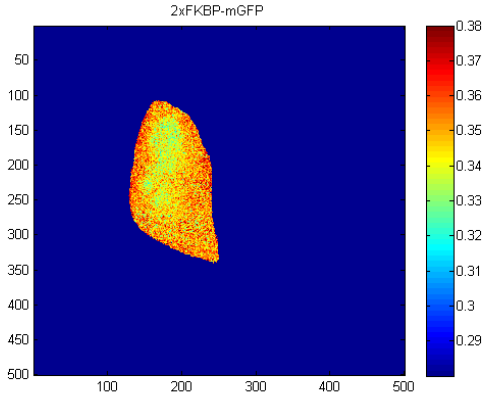
Figure 4.1: A typical anisotropy image of 2xFKBP-mGFP constructs. The anisotropy after selecting a region of interest and determining its average was found to be 0.339. The image is quiet smooth with a standard deviation of the mean value just below 0.01. The nucleus can clearly be recognized as an area with lower anisotropy since the autofluorescence of the nucleus is higher than from the cytoplasm.
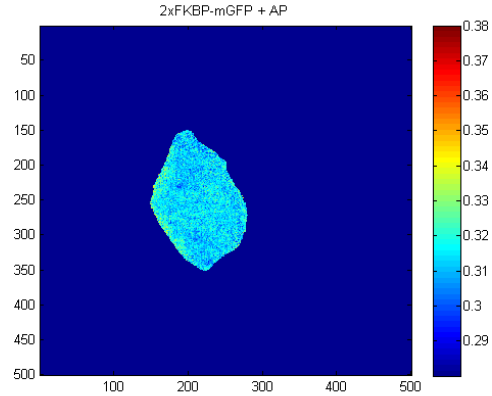
Figure 4.2: A typical anisotropy image of 2xFKBP-mGFP constructs upon addition of AP. The anisotropy was found to be 0.3165, again with a standard deviation of just below 0.01 for the average of the ROI, so again the image is smooth. The nucleus is harder to distinguish, but recognizable when comparing with the raw image. The nuclei of the cells were avoided when selecting ROIs because of their deviating anisotropy value.

reduction of resolution. A typical result of a measurement done with pixel binning is shown in figures 4.11 and 4.12, which show again threshold images for samples without and with addition of AP-20187 respectively. Clearly, the images are less smooth, so in fact relatively noisy, than the images that were acquired without binning. Moreover, the anisotropy decrease after addition of AP-20187 is smaller than in the former cases, as we conclude from the graph in figure 4.13 which shows a decrease of $4,4 \pm 2,2\%$, as displayed in 4.13. Moreover, the standard deviation in the anisotropy decrease is roughly twice as big as was the case for the non-binned images.

4.2.2 Uncertainty in the anisotropy

Usually, the noise due to photon statistics gives the highest contribution to the uncertainty in the anisotropy when doing (confocal) fluorescence microscopy, but in these experiments typical pixel values were 3000 to 6000 counts, yielding standard deviations lower than 0,02. This number was even further diminished by averaging over regions of interest of several thousands of pixels. Hence, the standard deviation due to photon statistics is negligibly small, only 10^{-3} - 10^{-4}.

For this moment we leave out the fundamental uncertainty that arises due to the error in the determination of the autofluorescence, on which we will elaborate later. The uncertainty in the anisotropy is determined by the variance in the actual pixel values, which is in fact a combination of all sources of uncertainty(photon statistics, quality of the registration, readout noise of the CMOS camera). We selected a region of interest to which we assigned a certain mean value. The standard deviation of this mean value of the ROI was calculated, using the
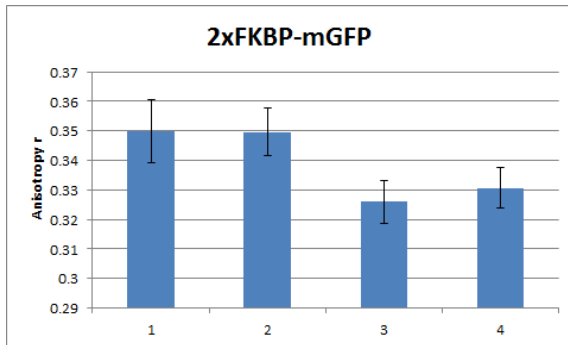
Figure 4.3: Anisotropy of the ROIs of the individually measured cells of 2xFKBP-mGFP with their standard deviation(in the order of $0,01$.

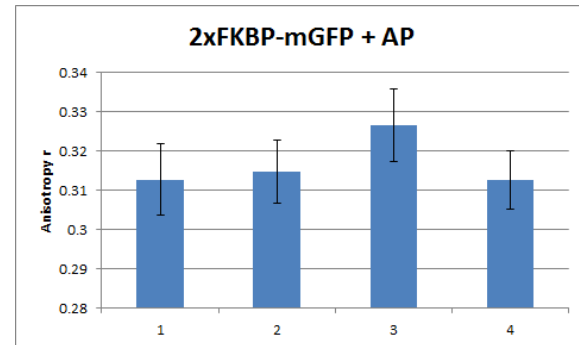Figure 4.4: Anisotropy of the ROIs of the individually measured cells of 2xFKBP-mGFP upon addition of AP20187 accompanied by the uncertainty of about $0,01$.
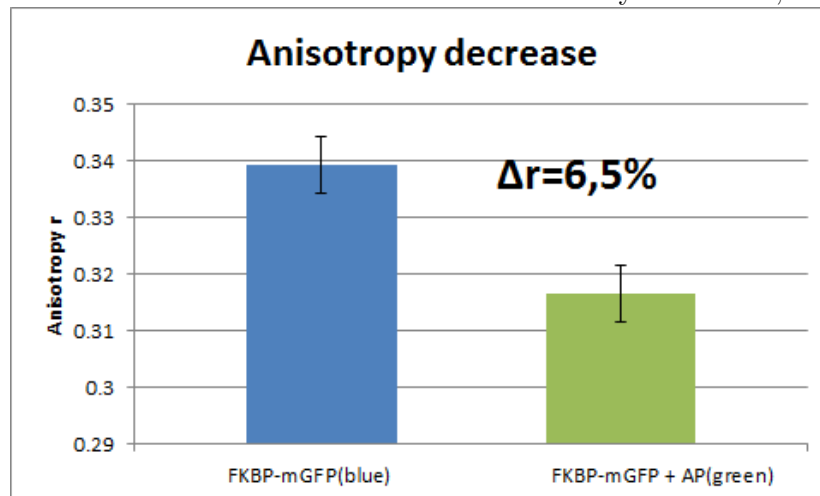

Figure 4.5: The difference of the anisotropy of 2xFKBP-mGFP constructs upon addition of the binding ligand AP20187 after averaging over all measured cells, yielding a lower standard deviation. The drop in anisotropy was found to be $6,5 \pm 1,2\%$.
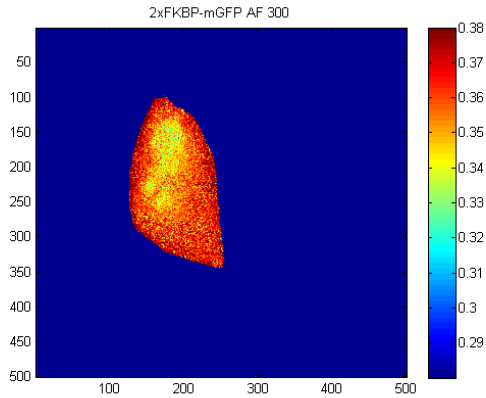
Figure 4.6: Anisotropy image of 2xFKBP-mGFP constructs after subtraction of a higher autofluorescence value. Clearly, the anisotropy is higher over the whole cell compared to figure 4.1, whereas the image remains smooth. The average anisotropy was found to be $0, 346$, roughly 2% higher.
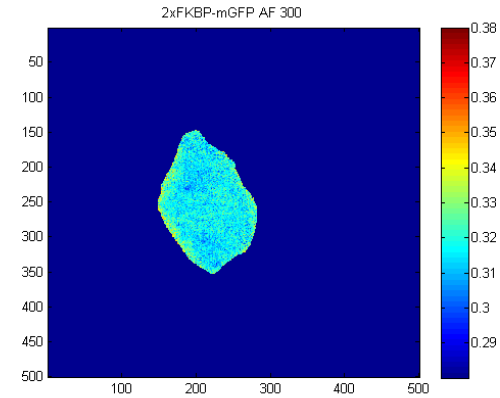
Figure 4.7: Anisotropy image of 2xFKBP-mGFP constructs upon addition of AP after subtraction of a higher autofluorescence value. The increase in anisotropy, averaged over all cells, with respect to 4.2 is again significant. A mean value of $0, 323$ was found, corresponding to an increase of 2%.
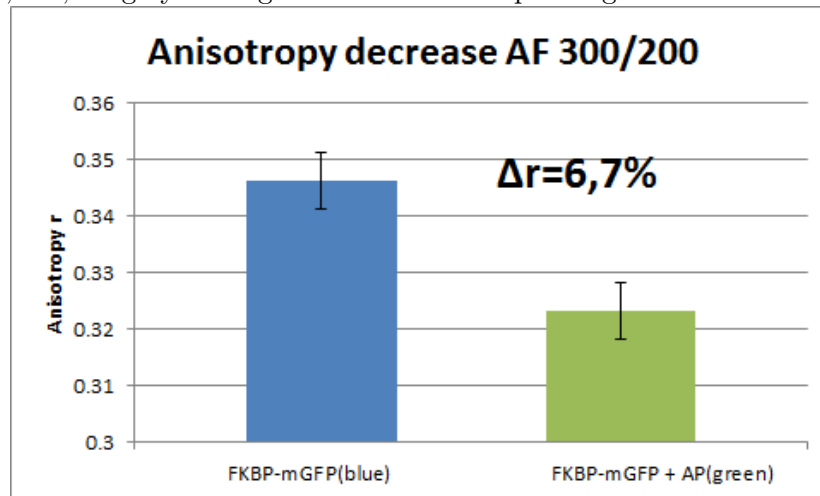

Figure 4.8: Difference of the anisotropy of 2xFKBP-mGFP constructs upon addition of the linker AP20187 for subtraction of a higher value of the autofluorescence(300/200). The drop in anisotropy was found to be $6, 7 \pm 1, 2\%$.
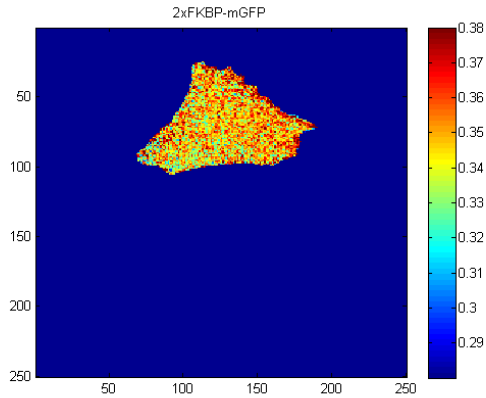
Figure 4.9: Anisotropy of 2xFKBP-mGFP arising from 2x2 pixels binned images. The average anisotropy of the ROIs was found to be $0,347$. The noisy character of the image indicates higher pixel value variations than was the case for the non-binned images(see figure 4.1), yielding a higher uncertainty of about $0,015$.
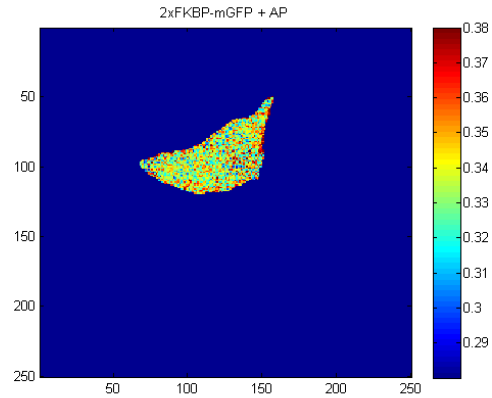
Figure 4.10: Anisotropy of 2xFKBP-mGFP + AP arising from 2x2 pixels binned images. The average over all cells was calculated to be $0,332$. Again, the image is rather noisy, compared to the non-binned images, with a standard deviation of $0,015$

commonl standard deviation of the mean(SDOM) formulas. Obviously, the anisotropy image of the binned images shows a higher standard deviation due to its noisy character. In case of the non-binned experiments, we found standard deviations of just below $0,01$ for the mean value of the individually measured cells. By averaging several measured cells, the standard deviation was further diminished to values around $0,005$. For the binned anisotropy images, typical values for the standard deviation of the individually measured cells were found to be slightly higher, around $0,015$(see figures 4.11 and 4.12), yielding standard deviations of the mean of $0,01$.

Of course, general propagation of uncertainty has been applied, as the individual uncertainties of the averaged anisotropy values for both constructs influence the accuracy of the final value of the anisotropy decrease due to clustering. Therefore, the higher uncertainty in the binned images causes a standard deviation wich is twice as big as in the case of non-binned images.
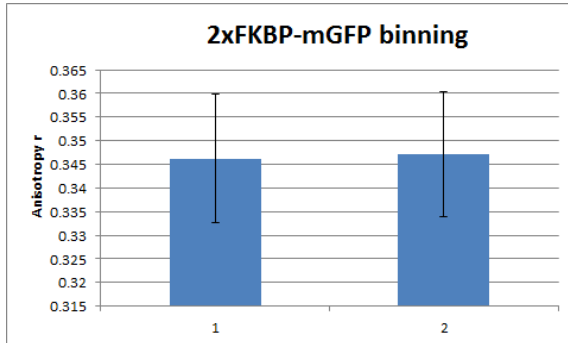
Figure 4.11: Anisotropy of the ROIs of the individually measured cells of 2xFKBP-mGFP. The standard deviation is significantly higher than for non-binned images due to the noisy character of the image.
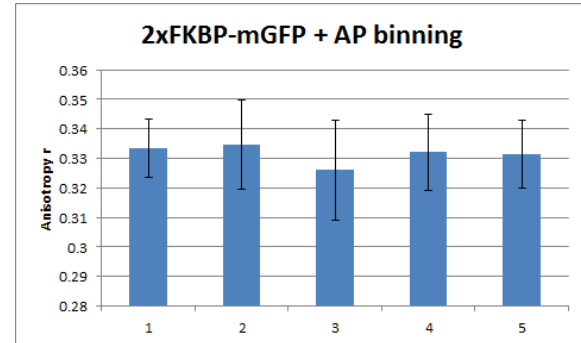

Figure 4.12: Anisotropy of the ROIs of the individually measured cells of 2xFKBP-mGFP upon addition of AP20187 accompanied by the uncertainty, which is higher than was the case in figure 4.4.
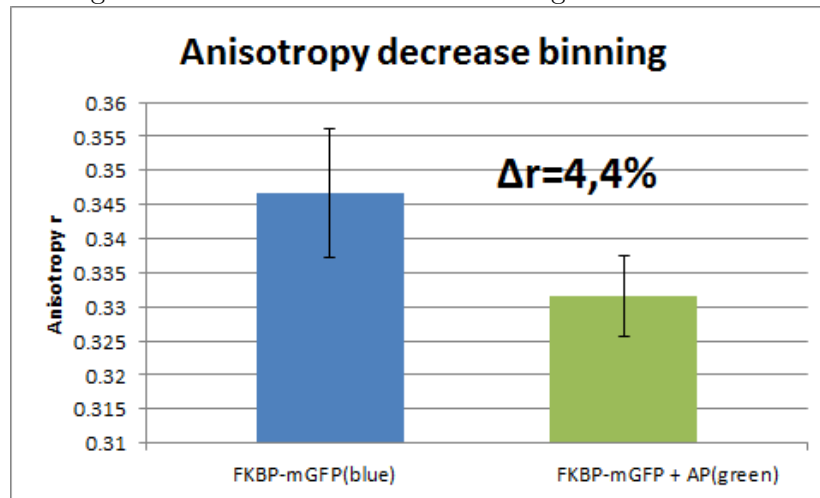

Figure 4.13: Difference of the anisotropy of 2xFKBP-mGFP constructs upon addition of the linker AP20187 for pixel binned images. The drop in anisotropy was found to be only $4,4 \pm 2,2\%$.

Chapter 5

Conclusion & Discussion

In this thesis, we provided a guideline for anisotropy measurements on a wide-field fluorescence microscope for simultaneous detection of the orthogonal emission polarizations. The key parameters in the assembly process of the microscope set-up, as well as a protocol for anisotropy measurements in wide-field anisotropy imaging were described. Furthermore, we performed measurements on biological samples in order to detect homo-FRET between GFP-proteins, hereby verifying if clustering of proteins has taken place.

The first step in the experimental procedure is the calculation of the G-factor. In order to ensure totally depolarized emission, the measurement on an aquaous fluorescein solution needs to be done without polarized excitation. Besides that, the signal-to-noise ratio is greatly enhanced by increasing the exposure time, typically 10 seconds, yielding uncertainties in the G-factor image of roughly 1% in our measurements, which is acceptable when considering propagation of this uncertainty in the anisotropy.
The maximum anisotropy of the system was determined by measuring GFP in glycerol. Clearly, the measurements are not satisfactory, since the obtained values were much lower than the values for GFP embedded in cells. However, analysis of the samples with a confocal microscope showed that the GFP molecules were stuck to the coverslip and so the measurements cannot be considered reliable. By using a blocking agent, for instance BSA, in the sample preperation, the GFP molecules can be prevented from getting stuck to the coverslip and so better results are to be expected.

The reference measurements on 2xFKBP-mGFP show a significant decrease in anisotropy upon addition of the binding ligand AP-20187, indicating clustering of the GFP molecules. Moreover, the smoothness of the images, with a spread of the pixel variation of about 0.01, indicates a proper registration of the parallel and perpendicular images. Therefore, these data can be taken reliable and confirm that the setup can discriminate between monomers(2xFKBP-mGFP) and oligomers(2xFKBP-mGFP + AP). However, though the drop in anisotropy of $6,5 \pm 1,2\%$ is significant, it is rather low compared to the results of [5], who found a difference of $14,9\%$ in steady-state confocal microscopy. Even a correction for the objective we used, $NA = 0.6$ whereas they used a $NA = 0.5$, would only account for a further drop in the anisotropy of 1 - 2% at maximum, according to figure 2.4.
The results of the binned images encounter the importance of the registration process. Although there still exists a significant, but lower, difference in the average anisotropies of

$4, 4 \pm 2, 2\%$ upon addition of the binding ligand, the images are quiet noisy, especially compared to the non-binned results. This results in an uncertainty which is about twice as big as the uncertainty in the non-binned anisotropy values. By binning the pixels upon imaging, obviously the resolution of the images is reduced, which in turn complicates the intensity-based registration process. Therefore, the quality of the registration diminishes and hence the overlaid parallel and perpendicular images might be mapped incorrectly, which most likely causes the noisy anisotropy images. If the resolution of the registration is not of the sub-pixel order, pixel A is subtracted from pixel B and so the anisotropy values are less reliable. Especially the fact that 200 nm fluorescent beads, which subtend an area of only 3-4 pixels squared, were used to determine the registration uncovers the complications of taking binned images.

Besides that, we saw that subtracting a slightly higher autofluorescence value, increases the anisotropies of both samples significant. For both the clustered and non-clustered samples we found an absolute anisotropy increase in the order of 2%. As the anisotropy of both samples increased with the same relative amount, the relative decrease in anisotropy hardly changed, only $0, 2\%$. However, the fact that slightly adjusting the autofluorescence contribution affects the absolute anisotropies that heavy, is important to consider. The estimation of the autofluorescence from unlabelled cells is not that easy as the variation in this signal is rather high. Obviously, the autofluorescence originating from the nucleus and the cytoplasm of the cell differ, but even within the cytoplasm itself, significant variations can be present due to the different cell components like the Golgi apparatus. As the increase of 2% in the absolute anisotropy upon subtracting a different autofluorescence value is relevant, a critical judgement of the actual value is needed in order to avoid wrong numbers and hence less satisfactory results.
Furthermore, the relatively low intensity cells show a bigger increase in anisotropy after subtraction of a higher autofluorescence value compared to the high intensity cells. This sounds logical since the relative contribution of a common background to the signal is higher for low-intensity cells than for high-intensity cells. However, this would suggest that the anisotropy is purely a function of the intensity. This was checked and only the increase in anisotropy upon subtraction of a higher autofluorescence background is intensity dependent, not the actual anisotropy. This implicates that samples of roughly the same intensity should be compared in order to avoid these issues.

Taking all these things together leaves us with the conclusion that the determination of the background autofluorescence is the most critical factor in wide-field anisotropy measurements, as other sources of uncertainty can be diminished properly by carrying out the experiments carefully. This could partly declare the difference in anisotropy decrease compared to measurements done in confocal microscopy, to which we referred, since the contamination from the background in confocal microscopy is greatly reduced with respect to wide-field. On the other hand, if the out-of-focus light present in wide-field microscopy carries useful information, it should be measured. Therefore, in addition, homo-FRET experiments could be carried out by using fluorescent dyes which emit in the red of the visible spectrum, as the autofluorescence of these cells should be significantly lower. An alternative way to overcome this limitation is exploring a method for computational deconvolution of the signal in order to obtain accurate focal sections, as discussed by[32]. In the latter case, the out-of-focus light which does provide useful information could be filtered instead of rejected(as occurs in confocal microscopy).

Acknowledgements

Probably, you would not be holding my thesis right now if it weren't for the help of and cooporation with many people. First of all, I would like to thank my daily supervisor Hans Gerritsen for his assistance over the last year. You taught me how to find the simplest possible interpretation of my data and always stressed me to keep in mind the practical side of doing research. Besides that, it's been a pleasure to me to explore and discuss our rivalry in soccer(PSV-AJAX) during the coffee breaks, which shows that it is not only science that matters.

I would also like to thank Dave van den Heuvel for introducing me to microscopy and guiding me through the practical sides of research, from which I really learned a lot. You were *always*, well in approximation, there to help me out when I experienced some technical problems during experiments. Moreover, you learned me to keep the spirits up when experiments fail and to enjoy my work. Furthermore, thanks for the fun we had during work and coffee breaks.

Also, I owe Gerhard Blab a big thanks for always helping me out on programming issues. Whenever I experienced a problem in MATLAB, ImageJ or LaTeX that was insolvable, at least in my opinion, you were there and easily solved it, leaving me stunned behind.

Thank you to my fellow room mates Hoa Truong, Helene Knaus and Tim van Werkhoven. It is a privilege to be able to work in such a great atmosphere like you offered. For the very same reason I'd like to thank Johan van Voskuilen. Though you have been working in Rotterdam for most of the time over the last months, you always lifted the atmosphere even higher when you were here.

In conclusion, it was a very big pleasure to spend the last year of my study life in this biophysics group. I will be remembering all the good laughs, the nice conversations and the superb atmosphere!

Bibliography

[1] V.M. Agranovich. Electronic excitation energy transfer in condensed matter. *North-Holland Publishing*, 1982.

[2] D. Altman. Precise positioning of myosin vi on endocytic vesicles in vivo. *PLoS Biol.*, 2007.

[3] D. Axelrod. Carbocyanine dye orientation in red cell membrane studied by microscopic fluorescence polarization. *Biophys. Soc.*, 1979.

[4] A.N. Bader. Imaging of protein cluster sizes by means of confocal time-gated fluorescence anisotropy microscopy. *Optics Express*, 2007.

[5] A.N. Bader. Homo-fret imaging enables quantification of protein cluster sizes with sub-cellular resolution. *Biophysical J.*, 2009.

[6] M. Born. *Principles of optics electromagnetic theory of propagation, interference and diffraction of light.* Pergamon Press, New York, 1980.

[7] A.H.A. Clayton. Dynamic fluorescence anisotropy imaging microscopy in the frequency domain(rflim). *Biophys. J.*, 2002.

[8] F.W. Craver. Theory of polarization quenching by excitation transfer ii. anisotropy and second-neighbour considerations. *Mol. Phys.*, 1971.

[9] W.H. De Vos. Four-dimensional telomere analusis in recordings of living human cells acquired with controlled light exposure microscopy. *J. of Microsc.*, 2010.

[10] J. De Vylder. 2d mapping of strongly deformable cell nuclei-based on contour matching. *Cytometry Part A*, 2011.

[11] J.P. Eichorst. Differential rhoa dynamics in migratory and stationary cells measured by fret and automated image analysis. *PLoS One*, 2008.

[12] A. Esposito. Fluorescence lifetime heterogeneity resolution in the frequency domain by lifetime moments analysis. *Biophys. J.*, 2005.

[13] T. Forster. Intermolecular energy migration and fluorescence. *Biological phys.*, 1993.

[14] T.W. Gadella. Oligomerization of epidermal growth factor receptors on a431 cells studied by time-resolved fluorescence imaging microscopy. a stereochemical model for tyrosine kinase receptor activation. *J. Cell Biology*, 1995.

[15] A. Gaudreau-Balderrama. Multi-modal image registration. *Boston University*, 2012.

[16] I. Gautier. Homo-fret microscopy in living cells to measure monomer-dimer transition of gfp-tagged proteins. *Biophys. J.*, 2001.

[17] D.J. Griffiths. *Introduction to Electrodynamics*. Prentice Hall, Englewood Cliffs, NJ, 1999.

[18] D.L. Hill. Medical image registration. *Physics in medicine and biology*, 2001.

[19] E.A. Jares-Erijman. Fret imaging. *Nat. Biotechnol.*, 2003.

[20] K.K. Jensen. enhanced uorescence resonance energy transfer between spectral variants of green uorescent protein through zinc-site engineering. *Biochemistry*, 2001.

[21] C.F. Kaminski. Homofret fluorescence anisotropy imaging as a tool to study molecular self-assembly in live cells, 2010.

[22] I.-H. Kim. Nonrigid registration of 2-d and 3-d dynamic cell nuclei images for improved classification of subcellular particle motion. *IEEE Transactions on image registration*, 2011.

[23] I.R. Lakowicz. *Principles of fluorescence spectroscopy*. Springer science+business media, LLC, 1983.

[24] I.R. lakowicz. Multiphoton excitation of biochemical fluorophores. *Topics in fluoresc. spectrosc.*, 1997.

[25] D.S. Lidke. Imaging molecular interaction in cells by dynamic and static fluoorescence anisotropy(rflim and emfret). *Biochem. Soc. Trans.*, 2003.

[26] K.A. Lidke. The role of photon statistics in fluorescence anisotropy imaging. *IEEE*, 2005.

[27] S. Oliveira. Molecular biology of epidermal growth factor receptor inhibition for cancer therapy. *Expert Opin Biol Ther*, 2006.

[28] A. Periasamy. *Methods in cellular imaging*. Oxford University Press, 2001.

[29] G.N. Phillips. Structure and dynamics of green uorescent protein. *Curr. Opin. Struct. Biol*, 1997.

[30] L.W. Runnels. Theory and application of fluorescence homo-transfer of melittin oligomerization. *Biophys. J.*, 1995.

[31] P. Sharma. Nanoscale organization of multiple gpi-anchored proteins in living cell membranes. *Cell*, 2004.

[32] P.J. Shaw. Comparison of widefield/deconvolution and confocal microscopy for three-dimensional imaging. 2005.

[33] W.T. Silfvast. *Laser Fundamentals*. Cambridge University Press, 2004.

[34] A. Sorkin. Endocytosis and intracellular trafficking of erbbs. *Exp Cell Res*, 2009.

[35] I.Z. Steinberg. Long-range nonradiative transfer of electronic excitation energy in proteins and polypeptides. *Annu. Rev. Biochem.*, 1971.

[36] L. Stryer. Fluorescence energy transfer as a spectroscopic ruler. *Annu. Rev. Biochem.*, 1978.

[37] J. Sytsma. Time-gated fluorescence lifetime imaging and microvolume dpectroscopy using two-photon excitation. *J. Microsc.*, 1998.

[38] B. Valeur. *Molecular Fluorescence. Principles and Applications.* Wiley-VCH, Weinheim, 2002.

[39] L.J. Van Vliet. Digital fluorescence imaging using cooled ccd array cameras. *Cell Biology*, 1998.

[40] F. Yang. The molecular structure of green uorescent protein. *Nat. Biotechnol.*, 1996.

[41] S. Yang. Nonrigid registration of 3-d multichannel microscopy images of cell nuclei. *IEEE Transactions on Image Processing*, 2008.

[42] D.A. Zacharias. partitioning of lipid-modied monomeric gfps into membrane microdomains of live cells. *Science*, 2002.

[43] B. Zitova. Image registration methods: a survey. *Image and vision computing*, 2003.

Appendices

Appendix A

Mathemetical considerations of anisotropy

A.1 Fundamental consideration of absorption and emission of a single molecule

The theoretical derivation of the anisotropy in terms of the parallel and perpendicular intensity, as given by equation 3, can be found by considering the absorption and emission features of a single molecule. For simplicity, let's assume a single molecule to have parallel adsorption and emission transition moments, without exhibiting rotational diffusion and that's oriented with angles θ and ϕ relative to the z-axis and y-axis relatively while performing z-axis symmetry, as depicted in figure.Furthermore, we assume the ground state of the molecules to be randomly oriented.

In figure A.1 we see the projections of the transition moment onto the axes. This projection is the same as the projection of the electric field of the fluorophore, which is given by[6, 17]

$$E(r, \theta, \phi) = k \frac{\sin \theta}{r} \hat{\theta} \tag{A.1}$$

where k is a constant, r is the distance to the fluorophore and $\hat{\theta}$ is the unit vector along the θ coordinate. Since the intensity is proportional to the square of the elctric field, the intensity distribution is given by

$$I(r, \theta, \phi) = k^2 \frac{\sin^2 \theta}{r^2} \hat{r} \tag{A.2}$$

where $\hat{r}$ is the unit vector in the direction of propagation.

Now we are able to derive the expressions for the parallel and perpendicular intensities by considering figure 2, whch depicts a dipole oriented the same as the fluorophore in figure 1. The electric field is always tangential to the field lines and around the equator, the electric field points in the same direction as the transition moment. Hence the projection onto the z-axis and x-axis are proportional to $\cos \theta$ and $\sin \theta \sin \phi$ respectively. As we now know the polarized intensity along an axis is proportional to the projection of the transition moments onto this axis, the parallel and perpendicular intensities are given by
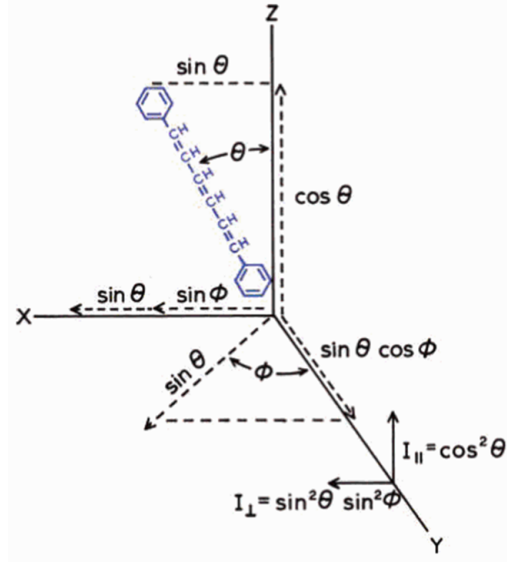
$$I_\|(\theta, \phi) = \cos^2 \theta \tag{A.3}$$

Figure A.1: Emission intensities of a fluorophore projected on the axes of a coordinate system[24]

$$I_\perp(\theta, \phi) = \sin^2 \theta \sin^2 \phi \tag{A.4}$$

Since we're dealing with randomly oriented fluorophores that are excited with polarized light, we need to calculate the contributions of different orientations to the measured intensities. For instance, upon excitation along the z-axis, all fluorophores with an angle ϕ with respect to the y-axis have an equal probability of being excited, i.e. the excited state populations is symmetrically distributed around the z-axis. This means that all values of ϕ, ranging from 0 to 2π, have equal absorption probabilities and hence the ϕ dependence can be eliminated from (A.4) by taking the average value of $\sin^2 \phi$

$$\langle sin^2\phi \rangle = \frac{\int_0^{2\pi} \sin^2 \phi \, \mathrm{d}\phi}{\int_0^{2\pi} \mathrm{d}\phi} = \frac{1}{2} \tag{A.5}$$

from which it follows that (A.4) becomes

$$I_\perp(\theta, \phi) = \frac{1}{2} \sin^2 \theta \tag{A.6}$$

Now, let's consider molecules oriented with a certain angle θ relative to the z-axis with a probability distribution of $f(\theta)$, which is important regarding the photo selective excitation and will be treated in the next section .Taking this probability distributions in account, the parallel and perpendicular intensities are given by

$$I_\parallel = \int_0^{\pi/2} f(\theta) \cos^2 \theta \, \mathrm{d}\theta = k\langle \cos^2 \theta \rangle \tag{A.7}$$

$$I_\perp = \frac{1}{2} \int_0^{\pi/2} f(\theta) \sin^2 \theta \, \mathrm{d}\theta = \frac{k}{2} \langle \sin^2 \theta \rangle \tag{A.8}$$

43

where $f(\theta)d\theta$ denotes the probability of finding a molecule oriented between an angle of θ and $\theta + d\theta$, and k is an instumental constant. If we now take the general formula for anisotropy and insert the goniometric identity $\sin^2\theta = 1 - \cos^2\theta$, we find

$$r = \frac{I_{pa} - I_{pe}}{I_{pa} + 2I_{pe}} = \frac{3\langle\cos^2\theta\rangle - 1}{2} \tag{A.9}$$

which reveals that the anisotropy, in case of fluorophores exhibiting z-axis symmetry, is only determined by θ, the angle of the emission dipole with respect to the z-axis. We see from (A.9) that complete loss of anisotropy occurs for $\theta = 54.7°$, which doesn't mean that each fluorophore is oriented with that angle, but rather it means that the average value of $\cos^2\theta$ is 1/3.

A.2 Theoretical maximum anisotropy

In the previous section we diddn't take into account the effect of photo selecive excitation on the anisotropy value. At first glance, you'd expect a maximum value of 1 for the anisotropy as follows from (A.9) when the transition moments are colinear, i.e. for $\theta = 0$. However, creating a perfectly oriented excited state population in a homogeneous solution is not possible. When a randomly oriented sample of fluorophores is illuminated with linearly polarized light, those fluorophores that have their absorption moments aligned with the excitation polarization have the highest probability of being excited. Meanwhile, molecules with slighty off-axis absorption will also be excited, but less efficient. In general, absorption is a quantum mechanical process where its transition probability relates to the initial state $|i\rangle$ and final state $|f\rangle$ by their coupling, which is described by Fermi's golden rule:

$$T = \frac{2\pi}{\hbar}|\langle f|H'|i\rangle|^2\rho_f \tag{A.10}$$

where ρ_f is the density of final states and $\langle f|H'|i\rangle$ is the bra-ket notation denoting the integral of the wavefunctions of the initial and final state over all space, $\int \psi_f^* H' \psi_i d\tau$, with H' the potential which causes the transition operating on the initial state wavefunction. The strength of the coupling is determined by this integral, so the stronger the coupling, the more likely the transition. This coupling strength is a function of the orientation of the fluorophore. Therefore, the probability of absorption is proportional to $cos^2\theta$[23], corresponding to the projection of the transition moment onto the z-axis in the former section. For this reason, we can only speak of a preferential oriented excited state population.

The number of molecules having angles between θ and $\theta + d\theta$ in a randomly oriented ground state distribution is proportional to $\sin\theta \, d\theta$. Hence, the probability distribution upon excitation by vertically polarized light is given by

$$f(\theta) \, d\theta = \cos^2\theta \sin\theta \, d\theta \tag{A.11}$$

From (A.9) we know that the anisotropy is determined by $\langle\cos^2\theta\rangle$, which in turn follows from the definition of a weighted mean

$$\langle\cos^2\theta\rangle = \frac{\int_0^{\pi/2}\cos^2\theta f(\theta)\,d\theta}{\int_0^{\pi/2}f(\theta)\,d\theta} \tag{A.12}$$
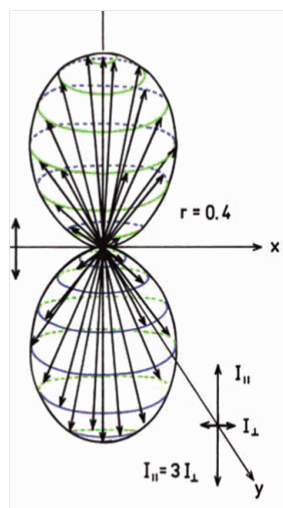
Figure A.2: Preferential excited state population caused by photo selective excitation yields a maximum anisotropy of $r = 0.4$

Substitution of (A.11) into (A.12) yields a value of 3/5 for $\langle \cos^2 \theta \rangle$ and hence the maximum anisotropy only reaches $r = 0.4$ for colinear absorption and emission dipoles and ignoring any other depolarizing factors, as depicted in figure A.2.

Appendix B

Implementation of computer codes

In this thesis we already referred to the use of programming within the data analysis process multiple times before. The majority of the analysis was done in MATLAB. Besides MATLAB, we used ImageJ to subtract background. The scripts we developed for both programs for the data analysis will be provided in this section.

B.1 Subtraction of background in ImageJ

```
// Allow the user to select an in- and output folder.
inputFolder = getDirectory("Choose input folder.");
outputFolder = getDirectory("Choose output folder");

// Create a list of all the files in this folder.
images = getFileList(inputFolder);

// Iniate for-loop, cycling through all files in folder.
for (i=0; i<images.length; i++) {
// The loop will open any files, including non-images. If you run into errors, remove the fo
// line, as well as in front of the curly bracket at the end of the loop.
    //if(endsWith(images[i], ".tif")) {
        // Define path to current image.
        inputPath = inputFolder + images[i];
        // A small progress bar in the FIJI interface. Just to show off.
        showProgress(i, images.length);
        // Open current image.
        open(inputPath);
        // Run subtraction on current image
        makeRectangle(0, 0, 500, 500);
        run("Crop");
        run("Subtract...", "value=210");
        run("32-bit");
        // Define place to save the file.
        outputPath = outputFolder + "BG corr " + images[i];
        // Save file...
```

```
27        saveAs("Tiff", outputPath);
28        // and close.
29        close();
30    //}
31  // Repeat ad infinitum.
32  }
```

B.2   Alignment of the images

```
1   function [tform, image_out, reg_out] = alignImages(image1, image2, optimizer, metric)
2
3   if ischar(image1)
4       image1=imread(image1);
5   end
6   if ischar(image2)
7       image2=imread(image2);
8   end
9
10  %dotpos=find(image2=='.');
11
12  % if (~isempty(dotpos))
13  %     image_out = [image2[1:(dotpos(end)-1)],'_warp.png'];
14  % else
15  %      image_out = [image2, '_warp.png'];
16  % end
17
18  if (nargin<4)
19      optimizer = registration.optimizer.RegularStepGradientDescent;
20      optimizer.MaximumIterations=500;
21      metric = registration.metric.MattesMutualInformation;
22  end
23
24  tform = imregtform(image2, image1, 'affine', optimizer, metric);
25
26  [image_out,reg_out] = imwarp(image2, tform,'OutputView',imref2d(size(image1)));
27
28  %% EOF
```

B.3   Calculation of the G-factor

```
1   function [g_val, imR]=calculateGfactor(imagep, images, tform)
2   % Function to calculate the G-factor after registering images
3
4   if nargin<2, help calculateGfactor; g_val=[]; return; end
5
```

```matlab
6    if ischar(imagep)
7        imagep=double(imread(imagep));
8    end
9    if ischar(images)
10       images=double(imread(images));
11   end
12
13   imR=imwarp(images, tform,'OutputView',imref2d(size(imagep)));
14
15   g_val = imagep./imR;
16
17   %% EOF
```

B.4   Calculation of the anisotropy

```matlab
1    function [image_ani, ave_ani, threshold, image_out, image1, tform] = calculateAnisotropy(ima
2    % help Nivard
3
4    if nargin<2, help calculateAnisotropy; image_ani=[]; ave_ani=0; threshold=[]; return; end
5
6    if nargin<4, g_val = 1; end
7
8    if ischar(image1)
9        image1=imread(image1);
10   end
11   if ischar(image2)
12       image2=imread(image2);
13   end
14
15    if (nargin<3 || isempty(tform))
16        [tform, image_out] = alignImages(image1, image2);
17    else
18        image_out=imwarp(image2, tform,'OutputView',imref2d(size(image1)));
19    end
20
21   im1= double(image1); im2=double(image_out);
22   image_ani = (im1 - g_val.*im2)./(im1 + 2*g_val.*im2);
23
24   threshold=image_ani; threshold(image1<1000)=0;
25
26   nonz=nonzeros(threshold);
27
28   ave_ani=nanmean(nonz);
29
30   %% EOF
```

B.5   Calculation of average of region of interest

```matlab
1  function [av, n]=Gemani(imtr,roi)
2
3  if nargin<2, help Gemani; return; end
4
5  av = mean(nonzeros(imtr.*roi))
6
7  n=size(nonzeros(roi))
8
9  %% EOF
```